



Vibration-based monitoring and diagnostics using compressive sensing[☆]



Vaahini Ganesan^{a,*}, Tuhin Das^b, Nazanin Rahnavard^c, Jeffrey L. Kauffman^b

^a Mech. & Aero. Engg. Dept., University of Central Florida, Orlando, FL, United States

^b Mech. & Aero. Engg. Dept., Univ. of Central Florida, Orlando, FL 32816, United States

^c Elec. & Comp. Engg. Dept., Univ. of Central Florida, Orlando, FL 32816, United States

ARTICLE INFO

Article history:

Received 26 August 2016

Received in revised form

13 January 2017

Accepted 1 February 2017

Available online 12 February 2017

Keywords:

Beam vibration

Sparsity

Compressive sensing

Fault detection

Signal recovery and reconstruction

ABSTRACT

Vibration data from mechanical systems carry important information that is useful for characterization and diagnosis. Standard approaches rely on continually streaming data at a fixed sampling frequency. For applications involving continuous monitoring, such as Structural Health Monitoring (SHM), such approaches result in high volume data and rely on sensors being powered for prolonged durations. Furthermore, for spatial resolution, structures are instrumented with a large array of sensors. This paper shows that both volume of data and number of sensors can be reduced significantly by applying Compressive Sensing (CS) in vibration monitoring applications. The reduction is achieved by using random sampling and capitalizing on the sparsity of vibration signals in the frequency domain. Preliminary experimental results validating CS-based frequency recovery are also provided. By exploiting the sparsity of mode shapes, CS can also enable efficient spatial reconstruction using fewer spatially distributed sensors. CS can thereby reduce the cost and power requirement of sensing as well as streamline data storage and processing in monitoring applications. In well-instrumented structures, CS can enable continued monitoring in case of sensor or computational failures.

© 2017 Elsevier Ltd. All rights reserved.

1. Introduction

Detecting and locating changes or faults in structures is an important field of research, as it has a direct impact on safety and reliability. During their service lifetime, structural components undergo and accumulate change in characteristics [1]. Early detection and location of these changes enable prolonged performance. In this regard, vibration-based monitoring is a well-established approach that is extensively documented in the literature [2]. Mechanical components such as shafts, wind turbine blades, etc. inevitably undergo vibrations in their operating environment. These vibrations inherently carry signatures in temporal and spatial domains that help indicate and locate changes in their characteristics [3,4]. Vibration-based detection methods are also popular in civil engineering structures such as bridges [5–7], for monitoring their structural health. A literature review of existing vibration-based monitoring and diagnostic techniques used in SHM is presented next.

Vibration-based SHM employs suitable in-situ active or passive transducers in order to analyze the characteristics of the structure in time, frequency, and modal domains [8–12]. Earliest approaches to this type of SHM involved comparison of

[☆] This work was supported by the National Science Foundation under Grant ECCS-418710.

* Corresponding author.

E-mail address: vaahini.ganesan24@gmail.com (V. Ganesan).

modal properties of the damaged structure against an undamaged baseline of the same structure. Areas of application include structures such as bridges and wind turbines [4–6,13,14]. All vibration-based SHM methods rely heavily on time-history response of a structure that can be acquired using sensors such as accelerometers, strain gauges, etc. Modal parameters are then extracted by transforming the response into frequency domain [15].

Looking more closely, detecting changes in the natural frequencies of a structure remains important in vibration-based SHM [2]. It was shown that with increasing severity of damage, natural frequencies exhibited a more distributed shift as opposed to localized shift [10,16,17]. The effect of the geometry of damage on the shift was studied in [18,19]. Sensitivity of frequency shifts to damage and ambient variations has also been of interest [20,21]. In addition, experimental validations have been conducted on actual structures [22–24]. Frequency Response Functions (FRF) have been utilized to determine natural frequencies and their shifts [25–27]. Here, fault localization is suggested by collecting the FRF from multiple sensors at different locations of the structure [8,28,29]. *The review indeed confirms that while the shifting of natural frequencies is an indicator of structural change, it is not an effective means of locating the same.* This brings the topic of spatial characterization in SHM.

Mode shape extraction from the response of structures, for detection and localization of damage, is also popular [15,30]. One technique is direct comparison between a specific mode shape of a structure in its healthy and damaged states using either Modal Assurance Criterion (MAC) or Coordinate Modal Assurance Criterion (COMAC) [31,32,14]. A disadvantage of mode shapes based SHM is the large amount of data that is required in order to make reliable and accurate detection [8]. Additionally, mode shape data is polluted by noise and measurement errors that affect their sensitivity to damage. A solution to by-pass this problem can be to measure the first (slope) or second (curvature) derivatives of the mode shape itself [33]. Nevertheless, the mode shape based SHM method is widely studied and applied in experiments as well [8,34–44]. A related method of extracting spatial information is by reconstructing the Operational Deflection Shapes (ODS) [45]. ODS are superposition of mode shapes and provide a physical view of the vibration of a structure [8,46]. Other approaches, such as the use of transmissibility for detecting structural change [47], and use of correlation coefficients to distinguish strain data [48] have been explored in literature.

Other related techniques for structural monitoring include Guided Wave Testing (GWT) [49], imaging and pattern recognition [50], and Wavelet transforms [51–55]. Spatial wavelet analysis for damage detection and localization is a recent approach that has gained popularity. However, inherent distortions in wavelet transform induces the possibility that damages near the boundaries of structures may be undetectable. In [56], the authors address this drawback by employing a novel padding method to the vibration response while using Continuous Wavelet Transform. While a plethora of techniques are now available for SHM, they mostly involve instrumenting a given structure with as many sensors as possible. Thereafter, data extraction follows the traditional approach of Nyquist-Shannon's sampling theorem [57]. Advancements in sensor systems and the drop in their costs have led to sensing proliferation, but at the expense of data volume, computational burden and power-requirement [58].

As mechanical and civil engineering structures become more complicated and their performance standards are raised, monitoring and diagnostics will increasingly become more challenging. Hence, in spite of faster computational speeds and superior sensor technologies, it is imperative that the efficiency of condition monitoring be improved. Higher efficiency of monitoring implies reduced sensing requirement, low computational burden, and a greater flexibility of sensing. In [59], the authors recognized the importance of down-sampling and investigated its effect on damage detection in the spatial domain. In this paper, the application of Compressive Sensing (CS) to vibration-based monitoring [60], is proposed in order to achieve reduced sensing. While this approach is still in its nascent stages, an important related work in literature is [61], where the authors evaluated the ability of CS to compress vibration data from civil structures. In [62], spatial interpolation of the impulse response of a vibrating plate using sub-nyquist sampling was investigated. Spatial sparsity may also be exploited for source localization of acoustic waves [63,64]. For data reduction, the combination of vibration-based monitoring and CS is optimal, since the former offers sparsity which the latter fundamentally requires. The approach is also less reliant on mathematical modeling and model-based computations. This paper develops the foundation for CS based monitoring for lateral vibration of beams. Fundamentals of lateral beam vibrations and the effect of structural changes are discussed in Section 2. Sparsity of vibrations and the motivation for using CS are discussed in Section 3. Examples of CS and quantitative comparison with Nyquist-Shannon sampling approach are given in Section 4. The use of CS in detecting change in natural frequencies is established and demonstrated through simulations in Section 5. Thereafter, spatial reconstruction of deflection-shape through CS and its application in locating a fault is shown in Section 6. Preliminary experimental validation of CS for detecting shift in natural frequencies is presented in Section 7 using a cantilever beam setup. The quality of spatial reconstruction is analyzed in Section 8. Finally concluding remarks with a note on future scope of this research are made and references are provided.

2. Fundamental characteristics of beam vibrations

Fundamentals of beam vibration can be extended to analyzing vibration of practical mechanical structures. Hence, the study of beam vibrations is imperative and key to the development of the proposed research. The vibration characteristics of beams in their operating environment change with progression of faults or other introduced structural changes. In Sections 2.1 and 2.2, we discuss the basics of beam vibrations and demonstrate changes in vibration characteristics through

simulations.

2.1. Lateral vibration response as weighted sum of modeshapes

The equation of motion of a uniform Euler-Bernoulli Beam is given by Eq. (1) [65]:

$$EI \frac{\partial^4 y(x, t)}{\partial x^4} + \rho A \frac{\partial^2 y(x, t)}{\partial t^2} = f(x, t) \tag{1}$$

where $y(x, t)$ is the lateral response of the beam, $f(x, t)$ represents forcing on the beam, E is the elastic modulus, I is the second moment of area, ρ is the density of the material and A is the area of cross section, all expressed in appropriate units. The response of the beam can be expressed as a weighted sum of its modeshapes as shown below,

$$y(x, t) = \sum_{q=1}^{\infty} T_q(t) W_q(x). \tag{2}$$

Here, the q th mode is represented by its mode shape $W_q(x)$, with principal co-ordinate $T_q(t)$, attached to it. In its most general form, $T_q(t)$ is influenced by both free and forced vibration components and can be expressed as [65]:

$$T_q(t) = A_q \cos(\omega_q t) + B_q \sin(\omega_q t) + \frac{1}{\rho A b \omega_q} \int_0^t Q_q(\tau) \sin(\omega_q(t - \tau)) d\tau$$

$$b = \int_0^L W_q^2(x) dx, \quad Q_q(t) = \int_0^L f(x, t) W_q(x) dx \tag{3}$$

In Eq. (3), A_q and B_q are constants obtained from initial conditions, L is the length of the beam, and ω_q is the q th natural frequency of vibration. Therefore, in effect, both free as well as forced vibration responses of a beam can be expressed as a weighted sum of mode shapes. Specifically, from Eqs. (2) and (3), the general structure of free vibration response of a beam is

$$y(x, t) = \sum_{q=1}^{\infty} [A_q \cos(\omega_q t) + B_q \sin(\omega_q t)] W_q(x) = \sum_{q=1}^{\infty} [\bar{A}_q(x) \cos(\omega_q t) + \bar{B}_q(x) \sin(\omega_q t)], \tag{4}$$

where $\bar{A}_q(x) = A_q W_q(x)$ and $\bar{B}_q(x) = B_q W_q(x)$. As expressed in Eq. (4), theoretically, the free vibration response of the beam is a combination of all its modes ($q = 1, 2 \dots \infty$). However, given an initial deflection profile, $y(x, 0)$, the modes present in that profile are manifested in the response. Similarly, the steady response of a beam to harmonic forcing $f = f_0 \sin(\omega_f t)$, applied at location x , takes the form

$$y(x, t) = \sum_{q=1}^{\infty} [D_q(\omega_q, \omega_f) f_0 \sin(\omega_f t)] W_q(x) = \sin(\omega_f t) \sum_{q=1}^{\infty} \bar{D}_q(\omega_q, \omega_f, f_0) W_q(x). \tag{5}$$

The expression $\sum_{q=1}^{\infty} \bar{D}_q(\omega_q, \omega_f, f_0) W_q(x)$ is the Operational Deflection Shape (ODS). The ODS is a constant shape that is maintained at any time when the operational forcing frequency remains unchanged. Furthermore, it is a linear combination of mode shapes $W_q(x)$ and predominantly contains those modes that lie in close proximity to the forcing frequency. Vibration response of a beam carries two types of signatures, namely: (i) natural frequencies ω_q in time domain, and (ii) mode shapes $W_q(x)$ in the spatial domain. A change in a beam's characteristics, for instance due to damage or deterioration, causes these signatures to change. Vibration-based monitoring of structures rely on detecting and quantifying these changes. Section 2.2 illustrates how structural changes or faults are manifested in natural frequencies, mode shapes and the ODS.

2.2. Identifying structural change using vibrational signatures

A finite-element simulation of a simply supported beam illustrates changes in vibrational characteristics. The structural parameters for the beam are assumed to be: $EI = 1, \rho A = 1, L = 5$ in consistent units. The beam is modeled using 100 elements

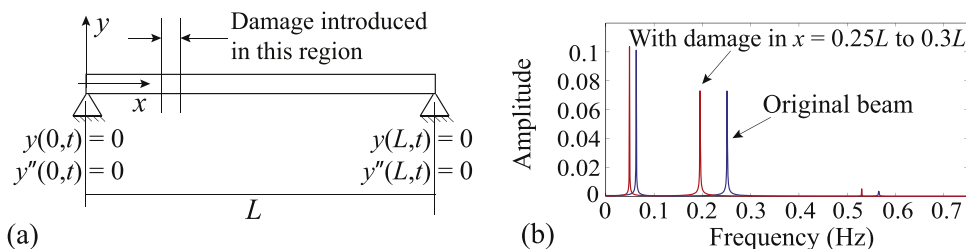


Fig. 1. (a) Uniform simply-supported beam, (b) Shift in natural frequencies due to damage.

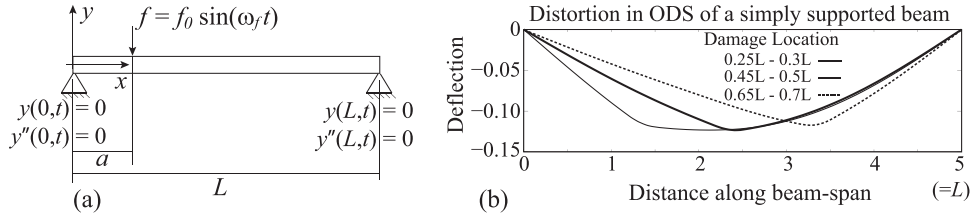


Fig. 2. (a) Uniform simply-supported beam under harmonic forcing, (b) ODS of beam showing distortions.

and simulated with boundary conditions of $y(0, t) = y(L, t) = y''(0, t) = y''(L, t) = 0$. A schematic is shown in Fig. 1(a). To demonstrate the change in characteristics, the value of EI was reduced from 1 to 0.1 in the region $0.25 \leq x \leq 0.3$, to simulate a damage. Shift in natural frequencies were extracted from free vibration response of the point $x = 0.75L$ using Fast Fourier Transform (FFT), and are shown in Fig. 1(b).

Frequency shift can be initial indicators of a developing change or damage in a beam. However, they are not a direct indicator of the location of the damage. The question of locating a damage can be addressed by the ODS.

To demonstrate this, the response of the simply-supported beam under a harmonic forcing of $f = \sin(0.5t)$ applied at $a = L/5$, as shown in Fig. 2(a), was simulated. Faults were introduced at different segments along the span of the beam. The resulting ODS, shown in Fig. 2(b), were generated for each damage scenario. The figure shows that the distortion in the ODS can indicate the location of a damage.

3. Sparsity in beam vibration and the application of compressive sensing

Consider the problem of recovering the natural frequencies and reconstructing ODS from vibration data of beams. This is of significance for detecting and locating structural damages. Traditionally, the vibration characteristics can be reconstructed from data using the Nyquist-Shannon Sampling Theorem [57]. According to this theorem, for good reconstruction of any given signal, the sampling frequency (f_s) has to be at least twice the highest frequency (f_b) contained in the signal, i.e., $f_s \geq 2f_b$. In practice, usually a much higher sampling rate is chosen, i.e. $f_s \gg 2f_b$. Traditional reconstruction algorithms such as the FFT relies on this sampling paradigm and results in high data volume when high frequencies are involved and high frequency resolution are needed. On the other hand, CS can allow signal reconstruction with significantly lower amount of data. It relies on sparsity of the signal in appropriate domain(s), a feature that is inherent in vibration of continuous systems.

Temporal Sparsity: Free vibration of any location on a beam is sparse in the frequency domain, since it only contains natural frequency harmonics. This is evident from Eq. (4). To illustrate sparsity, consider a beam vibrating with a combination of the first two natural frequencies ω_α and ω_γ . Their values are considered unknown but are known to lie in a range $\Omega_r = [0, \omega_r]$. Consider the task of recovering these frequencies from vibration data $z_i = y(\bar{x}, t_i)$ collected at a location \bar{x} on the beam using a series solution, i.e.

$$z_i = \sum_{j=1}^n [a_j \cos(\omega_j t) + b_j \sin(\omega_j t)], \quad \omega_j = \omega_r(j - 1)/(n - 1). \tag{6}$$

Conventionally, to determine $a_j, b_j, j = 1, 2, \dots, n$, we need $2n$ equations and hence $2n$ data points, implying $z = [z_1 z_2 \dots z_{2n}]^T$. Assuming that at indices $j=p$ and $j=p'$, $\omega_p = \omega_\alpha$ and $\omega_{p'} = \omega_\gamma$, we expect $a_j = b_j = 0 \quad \forall j \neq p, p'$. Thus, the vector $s = [a_0 a_1 \dots a_n \quad b_0 b_1 \dots b_n]^T$ has a sparsity of $k=4$. Fundamentally, this sparsity implies that data lesser than $2n$ should be sufficient to determine the constants $a_p, b_p, a_{p'}, b_{p'}$. CS capitalizes on this general idea of sparsity. By knowing that a signal is k -sparse, CS uses randomized and undersampled data, coupled with an ℓ_1 minimization algorithm, to find the sparse solution. This will be discussed in greater detail in Section 4.

Spatial Sparsity: As discussed in Section 2.2, ODS can be used to locate a damage/change in a beam. This requires spatial vibration data. ODS of beams also show sparsity, but in spatial-frequency domain. To explain this, note that the ODS $\sum_{q=1}^\infty \bar{D}_q(\omega_q, \omega_f, f_0) W_q(x)$, identified in Eq. (5), is a function of the mode shapes $W_q(x)$ only. The modes shapes in turn are functions of the spatial parameter β_q that are uniquely related to the natural frequencies ω_q . For instance, for uniform beams under lateral vibration $\omega_q = \beta_q^2 \sqrt{EI/\rho A}$, and a general expression of a mode shape is $W_q = C_q \sin(\beta_q x) + F_q \cos(\beta_q x) + G_q \sinh(\beta_q x) + H_q \cosh(\beta_q x)$, satisfying appropriate boundary conditions. The ODS thus takes the form

$$y_{ODS}(x) = \sum_{q=1}^\infty \bar{D}_q(\omega_q, \omega_f, f_0) W_q(x) = \sum_{q=1}^\infty \bar{C}_q \sin(\beta_q x) + \bar{F}_q \cos(\beta_q x) + \bar{G}_q \sinh(\beta_q x) + \bar{H}_q \cosh(\beta_q x), \tag{7}$$

which has a similar structure as Eq. (4), except it is in spatial domain with spatial frequencies β_q . The ODS, Eq. (7), is sparse in spatial-frequency since $\beta_q = f(\omega_q)$ and sparsity exists in the temporal frequency (i.e. ω) domain. This is the rationale for

applying CS to ODS reconstruction, which amounts to requiring fewer spatially distributed sensors. In addition to the ODS, free vibration of beams also shows spatial sparsity. This can be shown from Eq. (4). However, the deflection shape of free vibration varies with time. Thus, ODS is deemed a preferred candidate for spatial reconstruction, and for comparison with baseline data to locate faults.

4. Compressive sensing (CS)

4.1. An example of CS

CS deals with frequency recovery and reconstruction of an under-sampled signal from random, linear and non-adaptive measurements when the signal is sparsely represented in a proper basis [60]. The CS problem refers to finding a sparse solution $s \in R^n$, with sparsity k (i.e. with $\leq k$ nonzero entries), of the equation

$$\Phi s = z, \tag{8}$$

given a vector of measurements $z \in R^m$ and a measurement matrix $\Phi \in R^{m \times n}$ with $m < n$. The sparsest solution of the aforementioned under-determined set of equations is obtained from the l_0 minimization of s , which is NP-Hard to compute [60]. An alternative that is less computationally intensive is the l_1 minimization of s , which is given as

$$\hat{s} = \operatorname{argmin} \|s\|_{\ell_1} : \text{subject to } \Phi s = z, \tag{9}$$

where $\|s\|_{\ell_1} = \sum_{i=1}^n |s_i|$. The equivalence of the l_1 solution to l_0 is guaranteed under an additional condition on Φ , namely the *Restricted Isometry Property (RIP)* [66], which will be discussed in Section 4.2. The l_1 minimization is a convex optimization problem [67], and therefore easier to solve computationally. When the number of measurements m is of the order [68],

$$m \simeq O(k \ln(n/k)), \tag{10}$$

a carefully designed Φ satisfies RIP of order $2k$, thus allowing for the sparse solution to be obtained with overwhelming probability. In Eq. (10), k is the number of non-zero entries in s and hence represents its sparsity. While this result was originally derived for random matrices mostly, CS maybe extended to recovery of signals that have other types of expansions as well [68]. In the application to beam vibration, Φ is determined based on the beam response equation in temporal and spatial domains.

An example of frequency recovery using compressive sampling, from a given signal in time domain, is discussed next. Consider a signal $y(t)$ that can be expressed as $y(t) = \sum_{i=1}^n a_i \sin(\omega_i t)$. Further, assume that the vector $s = [a_1 \ a_2 \ \dots \ a_n]^T$ is k -sparse, i.e. only $k (< n)$ entries of s are non-zero. Let the corresponding frequency range for y be denoted by $\Omega_n \in [\omega_1, \omega_n]$. The CS problem, Eq. (8), can be posed as: *find the k -sparse solution s from m measurements of y , i.e. from $z_j = y(t_j)$, where $j = 1, 2, \dots, m$.* The vector $z = [z_1 \ z_2 \ \dots \ z_m]^T$ consists of measurements made at random instants, and $\Phi \in R^{m \times n}$ is constructed as $\Phi_{j,i} = \sin(\omega_i t_j)$. A lower bound on m is obtained from Eq. (10). Thus, Eq. (8) takes the form

$$z = \Phi s \Rightarrow \begin{bmatrix} z_1 \\ z_2 \\ \vdots \\ z_m \end{bmatrix} = \begin{bmatrix} \sin(\omega_1 t_1) & \sin(\omega_2 t_1) & \dots & \sin(\omega_n t_1) \\ \sin(\omega_1 t_2) & \sin(\omega_2 t_2) & \dots & \sin(\omega_n t_2) \\ \vdots & \vdots & \dots & \vdots \\ \sin(\omega_1 t_m) & \sin(\omega_2 t_m) & \dots & \sin(\omega_n t_m) \end{bmatrix} \begin{bmatrix} a_1 \\ a_2 \\ \vdots \\ a_n \end{bmatrix}$$

For this example, the following signal is considered, $y(t) = \sin(\pi t) - 0.5 \sin(4\pi t)$. In posing the CS problem, the frequency range considered is $\Omega_n \in [0, 2.5]$ Hz, $k=2$, the frequency resolution chosen is $\Delta f = 0.1$ Hz, implying $n=26$. Using the lower bound obtained from Eq. (10), we choose $m=7$. In Φ shown above, $\omega_i = (2\pi f_i)$ rad/s, where $f_i = [0, 0.1, 0.2 \dots 2.4, 2.5]$ Hz.

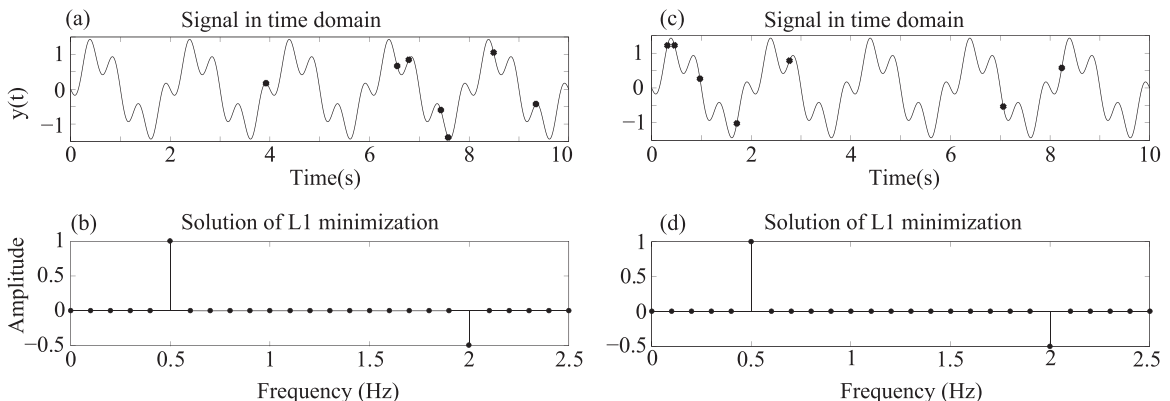


Fig. 3. Frequency recovery using Compressive Sampling from 2 Sets of Random Samples.

Fig. 3 illustrates two trials of frequency recovery using random sampling. The first trial is shown in Figs. 3(a) and (b), while the second one is depicted in Figs. 3(c) and (d). In each trial, the samples are randomly chosen and the ℓ_1 minimization is carried out using the ℓ_1 -magic code [69]. It can be observed that the desired frequencies are recovered at exact amplitudes in both the trials, irrespective of sample distribution. As mentioned above, the design of Φ is important for CS to be effective. To this end, Φ must satisfy a *Restricted Isometry Property*, explained in the next section.

4.2. Restricted isometry property (RIP)

The reconstruction of an under-sampled signal requires the design of a suitable measurement matrix Φ and that the signal be represented in a proper basis where it is k -sparse. For a high probability of reconstruction, Φ needs to satisfy the Restricted Isometry Property (RIP). A matrix Φ is said to satisfy RIP of order k if its *Restricted Isometric Constant* δ_k satisfies $0 < \delta_k < 1$. The constant δ_k is defined as the smallest value satisfying

$$(1 - \delta_k) \leq \frac{\|\Phi v\|_2^2}{\|v\|_2^2} \leq (1 + \delta_k), \tag{11}$$

for all vectors v with sparsity $\leq k$ [60]. Satisfying the RIP implies that all the column sub-matrices of Φ are well conditioned. These attributes lead to high probability of signal recovery by CS [60,66]. For a given k , δ_k for a matrix $\Phi \in R^{m \times n}$ can be determined numerically by applying the condition

$$(1 - \delta_k) \leq \lambda_{\min}(\Phi_T' \Phi_T) \leq \lambda_{\max}(\Phi_T' \Phi_T) \leq (1 + \delta_k) \tag{12}$$

for all sub-matrices $\Phi_T \in R^{m \times p}$ that can be formed from any p columns of Φ , with $1 \leq p \leq k$. In practice, however, $\delta_k \geq 1$ is not forbidden; it would simply mean that the stability of recovery under noise and the closeness of the ℓ_1 solution to ℓ_0 solution may not be well guaranteed [70].

In order to quantify RIP better, consider the example of Section 4.1. Since $k=2$ in this example, we need to determine δ_2 . For the given $m \times n$ (7×26) Φ matrix, we determined $\delta_2 = 0.95$. Thus $\delta_2 < 1$, and frequency recovery was reliable with high probability. Increasing the number of measurements m to 20 yielded $\delta_2 = 0.63$, which is expected. A lower δ_2 implies a higher probability of accurate frequency recovery. A third scenario, with $n=16$ and $m=7$, yielded $\delta_2 = 0.84$.

4.3. Quantitative comparison of CS and nyquist-shannon sampling theorem

For a quantitative comparison between CS and the traditional sampling, we consider the reconstruction of the following signal: $y(t)=\sin(0.3 \cdot 2\pi t) + 0.5 \sin(1.7 \cdot 2\pi t)$. In posing the CS problem, the frequency range considered is $\Omega_r \in [0, 2.5]$ Hz, $k=2$, and the frequency resolution chosen is $\Delta f = 0.1$ Hz, implying $n=26$. Using the lower bound obtained from Eq. (10), we choose $m=10$. In Φ shown above, $\omega_i = (2\pi f_i)$ rad s^{-1} , where $f_i = [0, 0.1, 0.2 \dots 2.4, 2.5]$ Hz. Fig. 4(a) illustrates the signal and the random samples. The ℓ_1 minimization was carried out using the ℓ_1 -magic code [69]. Frequency recovery through ℓ_1 minimization is shown in Fig. 4(b). It can be observed that correct frequencies and amplitudes are recovered from only 10 samples. To compare with traditional sampling, the above signal was sampled at 5 Hz, (so that Nyquist Frequency, 2.5 Hz, is greater than the highest signal frequency 1.7 Hz [71]). Three sets of data, i.e. 10, 20 and 50 samples, were used to carry-out

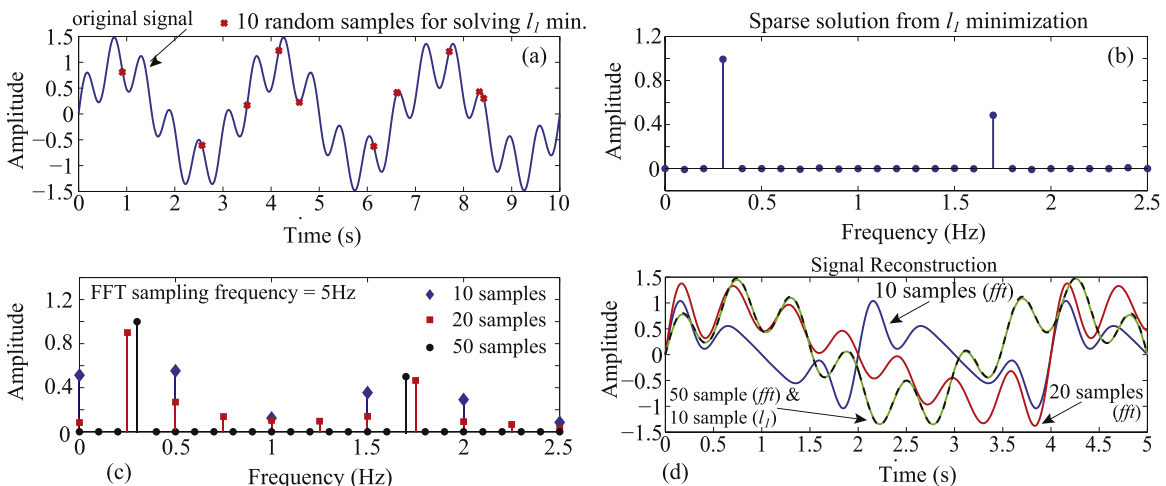


Fig. 4. (a) Signal and random samples, (b) Sparse solution from ℓ_1 optimization, (c) FFT of the signal with different number of samples, (d) Signal recovery with CS and FFT.

DFT (using the FFT algorithm). The consequent signal reconstruction in each of the three cases is achieved using those frequency components whose amplitudes are significantly above the noise level. The results are shown in Fig. 4(c) and (d). While the ℓ_1 minimization gave accurate reconstruction with 10 samples, the reconstruction had significant errors when traditional sampling technique was used, even with 20 samples. The accuracy of ℓ_1 -based reconstruction with 10 samples is at the same level as that of the reconstruction from FFT components with 50 samples.

The main differences between CS and FFT based approaches are:

1. Uniform vs. Random Sampling: The random sampling in CS effectively allows the data to be *richer* in information with fewer samples compared to regular sampling in FFT. In FFT this *richness* is achieved by increasing frequency and duration of sampling.

2. Exact vs. Probabilistic Solution: The FFT solution is exact in the sense that the quantity of data and the number of unknowns match. In contrast, ℓ_1 optimization fundamentally relies on sparsity and solves an under-determined system iteratively. This, combined with randomness of data, can assure recovery with a certain probability, albeit a very high one if RIP is satisfied by Φ .

3. Volume of Data: FFT fundamentally relies on high sampling rate for recovering a wide frequency-band and relies on high sampling duration for obtaining adequate resolution between neighboring frequencies. Both individually increase the data requirement proportionally. In CS, the data requirement is considerably more moderate, since it increases only with sparsity and in a logarithmic manner with the number of frequency components in Φ , Eq. (10).

4. Signal Sparsity: The ℓ_1 optimization relies on sparsity, and hence for sparse signals CS out-performs FFT. If signal sparsity is weak, the two methods may show comparable performance.

5. Frequency recovery from beam vibration

In Section 2.2, free vibration response of a beam was discussed, changes in natural frequencies and ODS were noted for changes in structural characteristics, and the sparsity of spatio-temporal vibration was discussed. This section explores the feasibility of using reduced number of (randomly placed) samples to recover the natural frequencies of vibration of mechanical beams using CS. This is investigated under two conditions: (i) When no changes have been introduced (unmodified or baseline) (ii) After changes have been introduced in the structure (modified). The following sections develop this method for simply supported and cantilever beams.

5.1. Detecting natural frequencies of a simply supported beam using CS

A simply supported beam has both its ends pinned and is constrained to have no displacement or bending moment on either ends, as shown in Fig. 5(a). We show the application of CS in detecting changes in its natural frequencies from free vibration data. A beam of length L is modeled with N_{el} finite elements, flexural rigidity EI , and mass density ρA . The free vibration response is simulated by providing an initial deflection profile $y(x, 0)$. As discussed in Section 2.1, the free vibration response will be dominated by those modes present in $y(x, 0)$. Hence, with the theoretical knowledge of baseline characteristics, the parameters for compressive sampling problem are set up following Section 4.1. The beam response thus obtained is compressively sampled to obtain baseline and modified natural frequencies $\omega_q, q = 1, 2, \dots$, and the shift in these frequencies allow detection of change in characteristics. From Eq. (4), considering that the q^{th} mode shape of a simply supported beam is $W_q(x) = \sin \frac{q\pi x}{L}$, and referring to Fig. 5(a), the free vibration response at a specified distance \bar{x} is given by

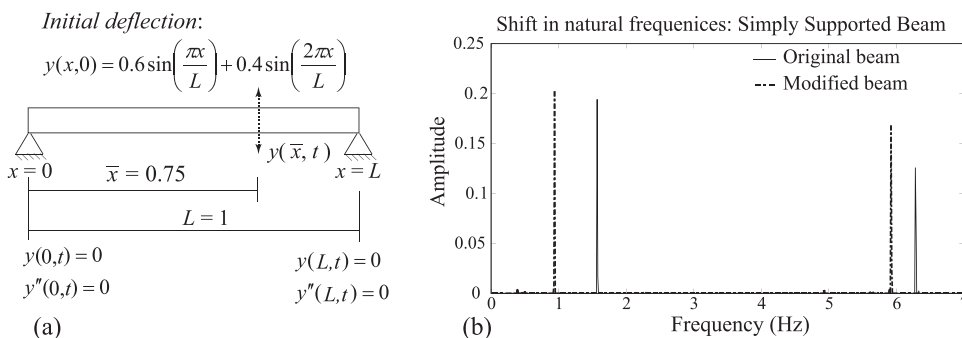


Fig. 5. (a) Schematic: Simply supported beam (b) Shift in natural frequencies: Recovery by CS from 15 random samples for each scenario.

$$\begin{aligned}
 y(\bar{x}, t) &= \sum_{q=1}^{\infty} (A_q \cos(\omega_q t) + B_q \sin(\omega_q t)) W_q(\bar{x}) = \sum_{q=1}^{\infty} (A_q \cos(\omega_q t) + B_q \sin(\omega_q t)) \sin \frac{q\pi\bar{x}}{L} \\
 &= \sum_{q=1}^{\infty} (\bar{A}_q(\bar{x})\cos(\omega_q t) + \bar{B}_q(\bar{x})\sin(\omega_q t)),
 \end{aligned}
 \tag{13}$$

where $\bar{A}_q(\bar{x}) = A_q \sin \frac{q\pi\bar{x}}{L}$ and $\bar{B}_q(\bar{x}) = B_q \sin \frac{q\pi\bar{x}}{L}$. The measurement point, \bar{x} , is chosen such that it does not fall at the nodal point (zero displacement point) of the response. In a realistic scenario, since multiple sensors will be spatially distributed, if a sensor location coincides with a node, alternate sensors can be used for CS based recovery. Consider the goal of recovering the natural frequencies ω_q using CS, within a frequency range of $\Omega_r \in [0, \omega_r]$. Further, consider a frequency recovery resolution $\Delta\omega$. The measurement vector $z \in R^m$ is generated from m random measurements $z_j = y(\bar{x}, t_j)$, $j = 1, 2, \dots, m$, and the matrix Φ is constructed using *sine* and *cosine* basis functions, Eq. (13). Since each frequency is represented by two basis functions, we expect even-sparsity in the solution of $s = [A'_1 \ A'_2 \ \dots \ A'_n \ B'_1 \ B'_2 \ \dots \ B'_n]^T$, $n = (\omega_r/\Delta\omega) + 1$, obtained from the ℓ_1 minimum solution of Eq. (8). In this case, Eq. (8) takes the form

$$\begin{aligned}
 z = \Phi s \quad \Rightarrow \quad \begin{bmatrix} z_1 \\ z_2 \\ \vdots \\ z_m \end{bmatrix} &= \begin{bmatrix} \cos(\omega_1 t_1) & \dots & \cos(\omega_n t_1) & \sin(\omega_1 t_1) & \dots & \sin(\omega_n t_1) \\ \cos(\omega_1 t_2) & \dots & \cos(\omega_n t_2) & \sin(\omega_1 t_2) & \dots & \sin(\omega_n t_2) \\ \vdots & & \vdots & \vdots & & \vdots \\ \cos(\omega_1 t_m) & \dots & \cos(\omega_n t_m) & \sin(\omega_1 t_m) & \dots & \sin(\omega_n t_m) \end{bmatrix} s \\
 \text{where } s &= [A'_1 \ A'_2 \ \dots \ A'_n \ B'_1 \ B'_2 \ \dots \ B'_n]^T.
 \end{aligned}
 \tag{14}$$

In Eq. (14), ω_i , with $i = 1, 2, \dots, n$, represent the spanning frequencies of the range Ω_r , i.e. $\omega_i = \Delta\omega(i - 1)$, $\omega_1 = 0$ and $\omega_n = \omega_r$. The ℓ_1 minimum sparse solution is referred to as \hat{s} , Eq. (9).

To demonstrate CS, a simply supported beam is considered with the following specifications: $L=1$, $\rho A = 1$, $EI=1$. The natural frequencies ω_q are $[\pi^2, 4\pi^2, 9\pi^2 \dots]$ in rad/s, and the corresponding mode shapes are $[\sin(\pi x), \sin(2\pi x), \sin(3\pi x), \dots]$ [65]. Free vibration is simulated using a discrete model consisting of $N_{el} = 500$ beam elements. It is given an initial deflection profile of $y(x, 0) = 0.6 \sin(\pi x/L) + 0.4 \sin(2\pi x/L)$, which is a combination of the first two mode shapes. This causes the first two natural frequencies to be manifested in the free vibration response. Typically, the proposed method can be applied to a wide variety of initial conditions and the corresponding modes will be manifested in the response. Change is introduced by reducing EI from 1 to 0.1 in the segment $0.4L \leq x \leq 0.5L$. The time domain response of the beam, before and after change, is measured at $\bar{x} = 3L/4$. The ℓ_1 minimization problem of Eq. (14) is setup with $\omega_r = 7 \text{ Hz} = 14\pi \text{ rad/s}$ and $\Delta\omega = 0.01 \text{ Hz} = 0.02\pi \text{ rad/s}$. This yields $n=701$ and we choose $m=15$ random measurements. This is comparable to $m=20$ suggested by Eq. (10), which is based on a sparsity of four for the first two natural frequencies. Note that the frequency range $\Omega \in [0, 7]$ is chosen to cover the first two natural frequencies $\omega_q = \pi/2 \text{ Hz}, 2\pi \text{ Hz}$.

The solutions of the two ℓ_1 minimization problems, namely before and after making changes in EI , are shown in Fig. 5. A schematic of the beam is shown in Fig. 5(a). Frequency recovery from data collected at $\bar{x} = 3L/4 = 0.75$ is shown in Fig. 5(b). The original natural frequencies $\omega_q = \pi/2 \text{ Hz}, 2\pi \text{ Hz}$ are correctly predicted by the ℓ_1 minimum solution. The amplitudes plotted are $\sqrt{A_i^2 + B_i^2}$, since each frequency ω_i has a combined basis function $[A'_i \sin(\omega_i t) + B'_i \cos(\omega_i t)]$, as evident from Eqs. (13) and (14). Fig. 5(b) also shows the shift in frequencies due to the change in EI . They were also determined by solving the same ℓ_1 minimization problem. The reduction in frequencies is expected since change was introduced in the form of reduction in EI (stiffness/rigidity).

To study the effectiveness of ℓ_1 minimization, we plot the accuracy of recovery as a function of the number of measurements m . The plot is shown in Fig. 6. The contour $k=2$ represents the normalized error norm $\|s - \hat{s}\|_2$ when only the 1st natural frequency $\frac{\pi}{2}$ Hz was present in the free vibration. The contour $k=4$ represents recovery when the 2nd natural

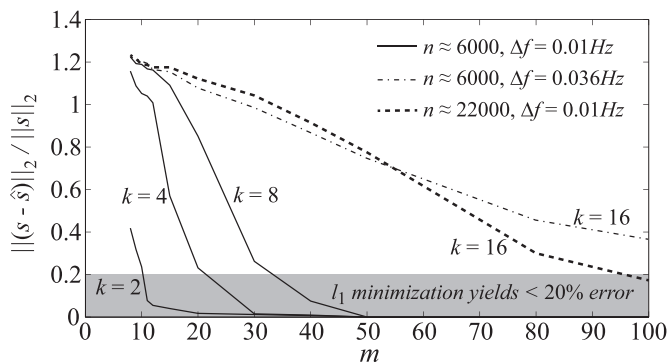


Fig. 6. Error analysis of ℓ_1 minimization as a function of measurements m for different signal sparsity.

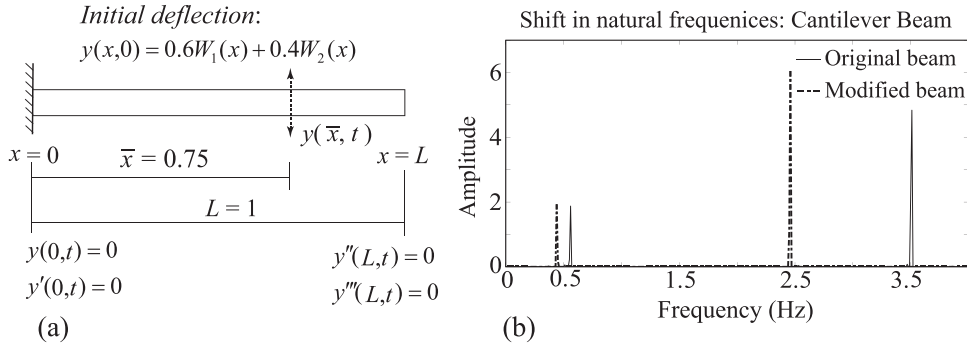


Fig. 7. (a) Schematic: Cantilever beam (b) Shift in natural frequencies: Recovery by CS from 15 random samples from each scenario.

frequency 2π Hz was superimposed with the 1^{st} . The contours $k=8$ and 16 similarly show the quality of recovery when the first 4 and first 8 natural frequencies respectively are present.

Nominally $n \approx 6000$ and $\Delta f = 0.01$ Hz was chosen, thus the frequency range of recovery was 60 Hz. This range contains the first six natural frequencies (recall that the n th natural frequency is $(n^2\pi/2)$ Hz). For $k=16$, the natural frequency $\omega_q = 32\pi > 60$ Hz, and hence Δf was increased to 0.036 Hz. For comparison n was increased to $n \approx 22000$, to restore $\Delta f = 0.01$ Hz. This improved the quality of recovery, as is evident in Fig. 6. Also, the number of measurements required to achieve higher accuracy of reconstruction increases with an increase in the number of frequencies to be recovered from the response. This is in accordance with Eq. (10). Because the number of measurements m , is affected by the natural logarithm of n , for a given value of sparsity k , an increase in n causes a modest increase in the value of m in contrast to a linear or exponential increase. In addition, it may be observed from Fig. 6, that there is a significant reduction in error when the lower bound on m is achieved.

5.2. Detecting natural frequencies of a cantilever beam using CS

A cantilever beam has one fixed end and one free end. The fixed end is constrained to have no displacement or slope during vibration. The free end experiences no bending moment or shear force. Similar to Section 5.1, here we show the application of CS in recovering the natural frequencies from vibration data collected from a single location. By detecting shifts in the frequencies, CS is used to predict changes in structural characteristics, such as damage. In this section, the approach is demonstrated using simulations. A cantilever beam is illustrated in Fig. 7(a). Its q^{th} mode shape is given by

$$W_q(x) = [\sin(\beta_q x) - \sinh(\beta_q x)] - \alpha_q [\cos(\beta_q x) - \cosh(\beta_q x)]$$

$$\cos(\beta_q L) \cdot \cosh(\beta_q L) = -1, \quad \alpha_q = \frac{\sin(\beta_q L) + \sinh(\beta_q L)}{\cos(\beta_q L) + \cosh(\beta_q L)}. \quad (15)$$

The solutions of β_q , from the above equation, are: $\beta_q L = [1.875, 4.694, 7.855, \dots]$ [65]. The free vibration response at a distance \bar{x} , as indicated in Fig. 7(a), is given by

$$y(\bar{x}, t) = \sum_{q=1}^{\infty} (A_q \cos(\omega_q t) + B_q \sin(\omega_q t)) W_q(\bar{x}) = \sum_{q=1}^{\infty} (\bar{A}_q(\bar{x}) \cos(\omega_q t) + \bar{B}_q(\bar{x}) \sin(\omega_q t)), \quad (16)$$

where $\bar{A}_q(\bar{x}) = A_q W_q(\bar{x})$ and $\bar{B}_q(\bar{x}) = B_q W_q(\bar{x})$, and the natural frequencies ω_q satisfy $\omega_q = \beta_q^2 \sqrt{EI/\rho A}$. The structure of Eq. (16) is similar to that in Eq. (13) and thus Eq. (14) is applicable to setup the ℓ_1 minimization problem for CS-based frequency recovery.

The specifications of the cantilever beam are identical to that of the simply-supported beam in Section 5.1, i.e. $L=1$, $\rho A = 1$, $EI=1$. The natural frequencies ω_q are $[3.52, 22.03, 61.7, \dots]$ in rad/s. Free vibration is simulated using a discrete model consisting of $N_{el} = 500$ beam elements. It is given an initial deflection profile of $y(x, 0) = 0.6W_1(x) + 0.4W_2(x)$, i.e. a combination of the first two mode shapes. This causes the first two natural frequencies to be manifested in the free vibration response. Change is introduced by reducing EI from 1 to 0.1 in the segment $0.4L \leq x \leq 0.5L$. The time domain response of the beam, before and after change, is measured at $\bar{x} = 3L/4$ and random measurements are made. The ℓ_1 minimization problem is setup with $\omega_r = 4$ Hz = 8π rad/s and $\Delta\omega = 0.01$ Hz = 0.02π rad/s. This yields $n=401$ and we choose $m=15$ random measurements. This is comparable to $m=18$ suggested by Eq. (10), which is based on $k=4$ for recovering two natural frequencies. Successful recovery of the vibrational frequencies using the CS methodology can be seen in Fig. 7(b). Reducing EI led to reduction of natural frequencies from $\omega_1 = 0.56$ Hz and $\omega_2 = 3.51$ Hz to 0.44 Hz and 2.45 Hz respectively. This was first determined numerically using the finite-element beam model. Subsequently, it was confirmed that the changes were reflected in ℓ_1 solution, as evident in Fig. 7(b).

6. Reconstruction of deflection shapes using CS

Section 2.2 illustrates that changes in beam characteristics produce distortions in its ODS. Determining the spatial response or the ODS is key to locating these changes. This section investigates reconstruction of the ODS of a beam using CS by applying it spatially. The deflection shape of a beam under free vibration, at an instant \bar{t} , can be expressed in terms of the normal modes $q = 1, 2, \dots, \infty$ as

$$\begin{aligned}
 y(x, \bar{t}) &= \sum_{q=1}^{\infty} [A_q \cos(\omega_q \bar{t}) + B_q \sin(\omega_q \bar{t})] W_q(x) \\
 &= \sum_{q=1}^{\infty} C_q(\bar{t}) W_q(x),
 \end{aligned}
 \tag{17}$$

where $C_q(\bar{t}) = [A_q \cos(\omega_q \bar{t}) + B_q \sin(\omega_q \bar{t})]$ and W_q is the q th mode shape. On the other hand, the steady response of a beam to harmonic forcing $f = f_0 \sin(\omega_f t)$, applied at location x takes the form of Eq. (5). From Eqs. (17) and (5), one distinction of the two deflection shapes is that the former is dependent on \bar{t} , while the other is not, provided the forcing has a steady amplitude and frequency. The latter represents the ODS. It is time-invariant and will be the focus of deflection reconstruction. The rationale for formulating the deflection shape reconstruction using compressive-sensing is that mode shapes W_q are sparse in β_q , since β_q and ω_q are related by $\omega_q = \beta_q^2 \sqrt{EI/\rho A}$. For instance for a simply-supported beam, $W_q = \sin \beta_q x = \sin \frac{q\pi x}{L}$ and that for a cantilever beam are given by Eq. (15). The following sections explain and illustrate ℓ_1 minimum solutions for reconstructing deflection shapes for simply-supported, fixed-fixed and cantilever beams. The emphasis will be on reconstruction from forced vibration response.

6.1. Deflection shape reconstruction for simply supported beam

Spatial recovery remains essentially similar to that of time-domain frequency recovery. The only difference being, sampling of the beam response is performed at one time instant from different spatial points along the length of the beam. In essence, the length axis becomes analogous to time axis. The parameters used to define the beam, L, EI and ρA , are the same as those in Section 5.1. Results of CS based recovery are validated against a finite-element model of the beam of N_{el} elements. Fig. 8(a) illustrates the beam. From Eq. (5), the deflection equation for a simply supported beam can be expressed as

$$y(x, \bar{t}) = \sum_{q=1}^{\infty} \bar{D}_q(\bar{t}) W_q, \quad W_q = \sin(\beta_q x) = \sin \frac{q\pi x}{L}.
 \tag{18}$$

Thus, the basis functions are sinusoids of wavelengths $\lambda_q = 2L/q$, i.e. of spatial frequency $\xi_q = q/2L$. Consider the problem of reconstructing the deflection shape of the beam under a harmonic force with frequency $\omega_q < \omega_f < \omega_{q+1}$. The deflection shape will be dominated by the q th and $(q + 1)$ th mode shapes, i.e. by ξ_q and ξ_{q+1} . Consider a spatial frequency range $\Xi_r = [\xi_l, \xi_h]$, such that $(\xi_q, \xi_{q+1}) \in \Xi_r$, and a measurement vector $z \in R^m$ generated by measurements y taken at m random locations along the length of the beam at an instant \bar{t} , $z_j = y(x_j, \bar{t})$, $j = 1, 2, \dots, m$. Writing z_j as

$$z_j = \sum_i^n H_i \sin(2\pi \xi_i x_j), \quad \xi_i = \xi_l + (i - 1) \frac{(\xi_h - \xi_l)}{n - 1}, \quad i = 1, 2, \dots, n,
 \tag{19}$$

the deflection shape can be reconstructed by determining the ℓ_1 minimum solution of

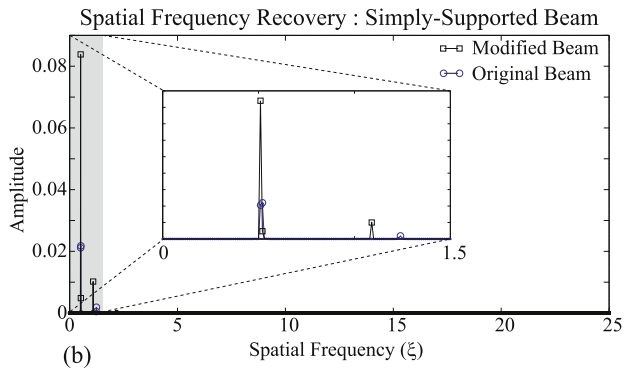
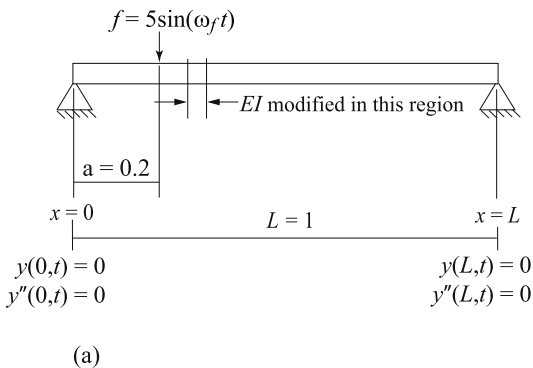


Fig. 8. (a) Schematic: Simply Supported beam with harmonic excitation (b) Spatial frequencies recovered before and after modification of elements.

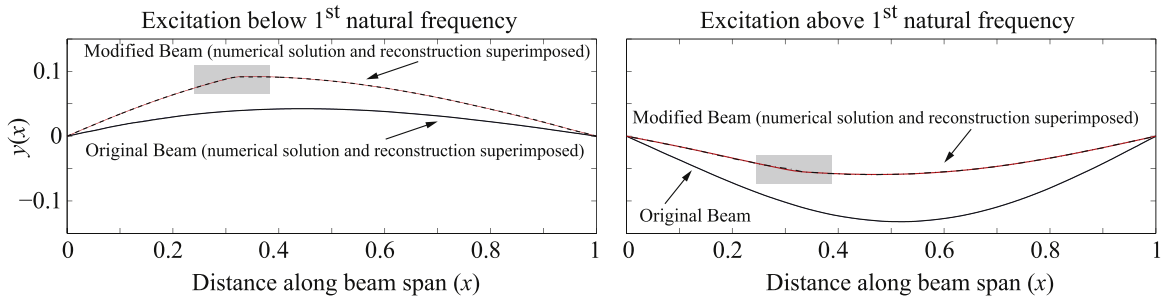


Fig. 9. Deflections of original and modified beam, with numerical solutions and reconstructed deflections superimposed: (a) ω_f below, and (b) ω_f above the 1st natural frequency.

$$z = \Phi s, \quad \Phi = \begin{bmatrix} \sin(2\pi\xi_1 x_1) & \sin(2\pi\xi_2 x_1) & \cdots & \sin(2\pi\xi_n x_1) \\ \sin(2\pi\xi_1 x_2) & \sin(2\pi\xi_2 x_2) & \cdots & \sin(2\pi\xi_n x_2) \\ \vdots & \vdots & \ddots & \vdots \\ \sin(2\pi\xi_1 x_m) & \sin(2\pi\xi_2 x_m) & \cdots & \sin(2\pi\xi_n x_m) \end{bmatrix},$$

$$s = [H_1 \ H_2 \ \cdots \ H_n]^T. \quad (20)$$

In Eq. (20), Ξ_r forms a searching frequency-range and we expect to obtain a sparse solutions with non-zero H_i if $H_i \approx \bar{D}_q$. We note that although the deflection shape will have the presence of other mode shapes, such as $(q - 1)^{th}$ and $(q + 2)^{th}$, but their influence will be minor. When the characteristics of the beam changes locally, such as due to damage, the mode shapes W_q cease to have the analytic form of Eq. (18). Hence in a damaged or modified beam, the ℓ_1 minimum solution will show a lower sparsity in general. However, an indicator of the location of a damage will be the reconstructed deflection shape itself rather than the non-zero coefficients of the sparse solution.

To illustrate the observations made above, we simulate forced vibration of a beam with the following parameters: $L=1$, $\rho A=1$, $EI=1$. For the simulation, a finite element model of the beam is used with $N_{el}=1000$. It is subject to a harmonic excitation force $F=5 \sin(5t)$, which is applied at a distance $a=0.2$ from the left, as shown in Fig. 8(a). In the original beam, the spatial frequencies ξ_q are 0.5, 1, 1.5, ..., and the corresponding natural frequencies ω_q are $\pi^2, 4\pi^2, 9\pi^2, \dots$ rad/s. Since $\omega_f = 5 < \pi^2$, the deflection shape is expected to be mostly dominated by its first mode. To reconstruct the deflection shape, $m=25$ random displacement samples were collected at a specific time-instant along the beam-span. The ℓ_1 minimum solution of Eq. (20) was determined with $n=2500$, $\xi_l=0$ and $\xi_h=25$, implying a frequency resolution of ≈ 0.01 , see Eq. (20). The sparse solution for the original beam is shown in Fig. 8(b), showing the dominant spatial frequency to be at the first mode shape $\xi=0.5$, as expected.

Next, a fault is introduced by reducing EI from 1 to 0.1, locally in the region $x \in [0.3, 0.35]$, and the ℓ_1 minimum solution was recalculated. The solution is indicated in Fig. 8(b) as modified beam. The ℓ_1 minimum solutions show shifts in spatial frequencies between the original and modified beam. However, they do not reflect the location of modification (or damage). To determine the location of the damage, the frequencies recovered are used to reconstruct the deflection shape. The reconstruction is shown in Fig. 9(a) for both the original beam and the modified beam. The accuracy of reconstruction is verified by superimposing the numerical solutions obtained from the finite element model. For further illustration of shape reconstruction, the forcing frequency was increased $\omega_f = 11$ rad/s, which is above the 1st natural frequency of the original beam. The CS problem was solved to determine the sparse solution in spatial domain and the deflection-shape was reconstructed using the same procedure as above. The results are shown in Fig. 9(b). In both Figs. 9(a) and (b), we notice that the region of the defect (or modification) is visually identifiable, and are indicated by the gray squares. In Fig. 9(a), it was better identifiable due to higher amplitude of oscillation resulting from lower excitation frequency. We clarify that the deflection directions are flipped in Fig. 9(a) and (b) simply because at the instants at which data were taken, the beams were undergoing positive and negative displacements respectively.

6.2. Deflection shape reconstruction for fixed-fixed beam

In this section, deflection shape reconstruction, using the idea of compressive sampling, is demonstrated for fixed-fixed beam. The process closely follows the one in Section 6.1. Both ends of a fixed-fixed beam are constrained to have neither displacement nor slope. The beam-parameters, L , EI and ρA , carry their usual meaning. As before, CS based recovery are validated against a finite-element model of the beam of N_{el} elements. Fig. 10(a) illustrates the beam. From Eq. (5) and [65], the deflection equation for a fixed-fixed beam, at an instant \bar{t} can be expressed as

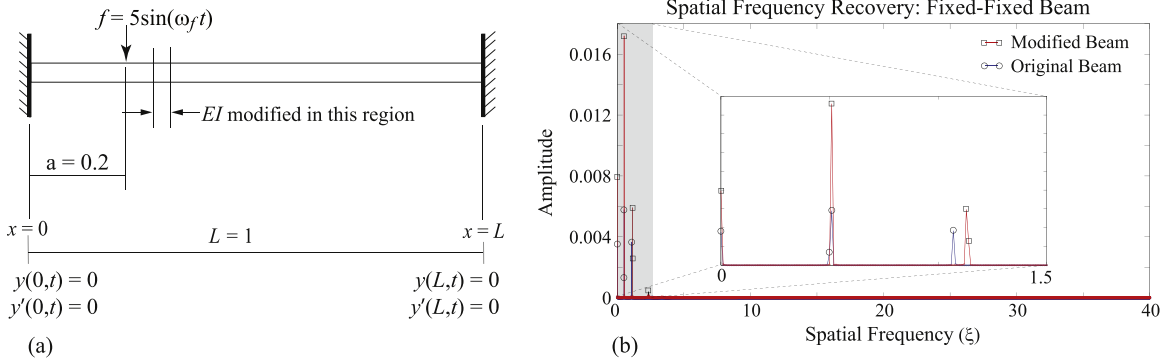


Fig. 10. (a) Schematic: Fixed-fixed beam with harmonic excitation (b) Spatial frequencies recovered before and after modification of elements.

$$y(x, \bar{t}) = \sum_{q=1}^{\infty} \bar{D}_q(\bar{t}) W_q, \quad W_q = (\sinh \beta_q x - \sin \beta_q x) + \alpha_q (\cosh \beta_q x - \cos \beta_q x),$$

$$\alpha_q = \frac{\sinh \beta_q L - \sin \beta_q L}{\cos \beta_q L - \cosh \beta_q L}, \quad \cos \beta_q L \cdot \cosh \beta_q L = 1. \tag{21}$$

Here the basis is formed by sinusoids and hyperbolic functions. The sinusoids have wavelengths $\lambda_q = 2\pi/\beta_q$, i.e. spatial frequency $\xi_q = \beta_q/2\pi$. For fixed-fixed beams, Eq. (21) yields $[\beta_1 L, \beta_2 L, \beta_3 L, \beta_4 L, \dots] = [4.73, 7.85, 11, 14.14, \dots]$.

Spatial reconstruction was formulated on similar lines as in Section 6.1. The following specifications were chosen for the beam: $L=1, \rho A = 1, EI=1$ and $N_{el} = 1000$. The beam is harmonically excited at $\omega_f = 20$ rad/s which is lower than the first natural frequency of the undamaged beam, $\omega_1 = \beta_1^2 = 22.37$ rad/s. The force, of amplitude 5, is applied at a distance $a=0.2$ from the left, as indicated in Fig. 10(a). The resulting ODS is expected to resemble a sinusoid of wavelength 2, i.e. $\xi = 0.5$, but with zero deflection and slope near the fixed ends. Structural change is introduced by a reduction in EI from 1 to 0.1 in the region $x \in [0.3, 0.35]$. The ℓ_1 minimization problem for deflection reconstruction requires a spatial frequency range, as done in Section 6.1. The range chosen for both the original and modified cases are $\Xi_r = [\xi_l, \xi_h] = [0, 40]$, with a resolution of 0.01. The measurement vector $z \in R^m$ is generated by taking $m=25$ measurements y taken at random locations along the length of the beam at an instant \bar{t} , $z_j = y(x_j, \bar{t})$, $j = 1, 2, \dots, m$. Based on Eq. (21), z_j can be expressed as a function of the basis functions as follows:

$$z_j = \sum_i^n [H_{i,1} \sin(2\pi\xi_i x_j) + H_{i,2} \sinh(2\pi\xi_i x_j) + H_{i,3} \cos(2\pi\xi_i x_j) + H_{i,4} \cosh(2\pi\xi_i x_j)],$$

$$\xi_i = \xi_l + (i - 1) \frac{(\xi_h - \xi_l)}{n - 1}, \quad i = 1, 2, \dots, n, \tag{22}$$

or in a more condensed form, based on Eq. (21) as,

$$z_j = \sum_i^n H_i [(\sinh(2\pi\xi_i x_j) - \sin(2\pi\xi_i x_j)) + \alpha_i (\cosh(2\pi\xi_i x_j) - \cos(2\pi\xi_i x_j))]$$

$$\alpha_i = \frac{\sinh(2\pi\xi_i L) - \sin(2\pi\xi_i L)}{\cos(2\pi\xi_i L) - \cosh(2\pi\xi_i L)}. \tag{23}$$

However, trial runs showed poor reconstruction when either of the above sets were used. In contrast, upon using the sine and cosine functions only

$$z_j = \sum_i^n [H_{i,1} \sin(2\pi\xi_i x_j) + H_{i,2} \cos(2\pi\xi_i x_j)], \tag{24}$$

resulted in significantly better reconstruction. Specifically, the deflection shape was reconstructed by determining the ℓ_1 minimum solution of

$$z = \Phi s, \quad \Phi = \begin{bmatrix} \sin(2\pi\xi_1 x_1) & \dots & \sin(2\pi\xi_n x_1) & \cos(2\pi\xi_1 x_1) & \dots & \cos(2\pi\xi_n x_1) \\ \sin(2\pi\xi_1 x_2) & \dots & \sin(2\pi\xi_n x_2) & \cos(2\pi\xi_1 x_2) & \dots & \cos(2\pi\xi_n x_2) \\ \vdots & \vdots & \vdots & \vdots & \vdots & \vdots \\ \sin(2\pi\xi_1 x_m) & \dots & \sin(2\pi\xi_n x_m) & \cos(2\pi\xi_1 x_m) & \dots & \cos(2\pi\xi_n x_m) \end{bmatrix},$$

$$z \in R^m, \quad s = [H_{1,1} \ H_{2,1} \ \dots \ H_{n,1} \ H_{1,2} \ H_{2,2} \ \dots \ H_{n,2}]^T. \tag{25}$$

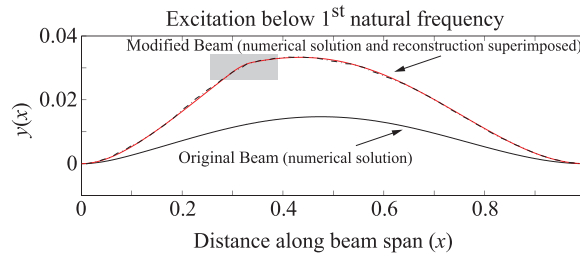


Fig. 11. Deflections of original and modified beam with superimposed reconstruction.

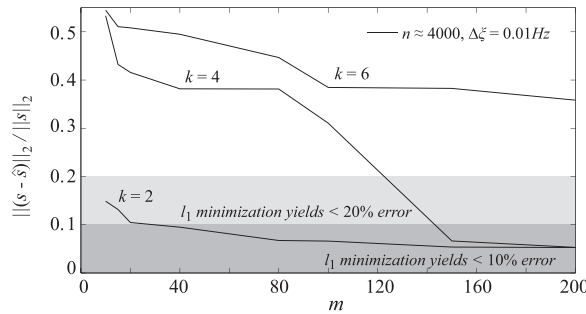


Fig. 12. Error analysis of ℓ_1 minimization as a function of measurements m for different spatial signal sparsity.

The reason the formulations of Eqs. (24) and (25) perform better than those in Eqs. (22) and (23) is better understood by comparing the *Restricted Isometry Constant* for each case for similar sparsity. As explained in Section 4.2, this constant is a measure of how well-conditioned the corresponding Φ matrix is. A numerical comparison of the constant, calculated for different sets of basis functions, will be discussed in Section 8. Fig. 10(b) shows the sparse solution obtained by ℓ_1 minimization. For each frequency, the amplitude is calculated as $\sqrt{H_{r1}^2 + H_{r2}^2}$. Because the deflection shape is similar to a sinusoid but with zero slopes at the ends, a constant amplitude component is also recovered. In addition to this, the fundamental spatial frequency $\xi = 0.5$ is also prominent. Locating a change/damage requires comparison of the deflection shape before and after introducing structural change in the beam. The reconstructed deflection shape of the modified beam (with EI reduced from 1 to 0.1) is superimposed with the numerical solution in Fig. 11. Numerical solution of the original deflection is shown on the same plot.

Recall Fig. 6, where the effectiveness of ℓ_1 minimization was studied by plotting the accuracy of signal recovery in the temporal domain against the number of measurements m . Fig. 12 illustrates the same, but signal recovery is in the spatial domain for the unmodified fixed-fixed beam described above. In this domain, recovery of spatial frequencies is considered and the signal sparsity is determined by the number of spatial frequencies present in it. Nominally, $n \approx 4000$ and $\Delta\xi = 0.01$ was chosen, thus the frequency range of recovery was $\Xi_r = [0, 40]$. Although the highest spatial frequency expected to be recovered is less than 2, this extended frequency range is important for inducing sparsity in the signal, thereby ensuring good deflection reconstruction.

The contour $k=2$ represents the normalized error norm $\|s - \hat{s}\|_2$ when the forced vibration response of the fixed-fixed beam was dominated by the 1st mode, $\xi \approx 0.5$. The contour $k=4$ represents accuracy of recovery when the first two modes

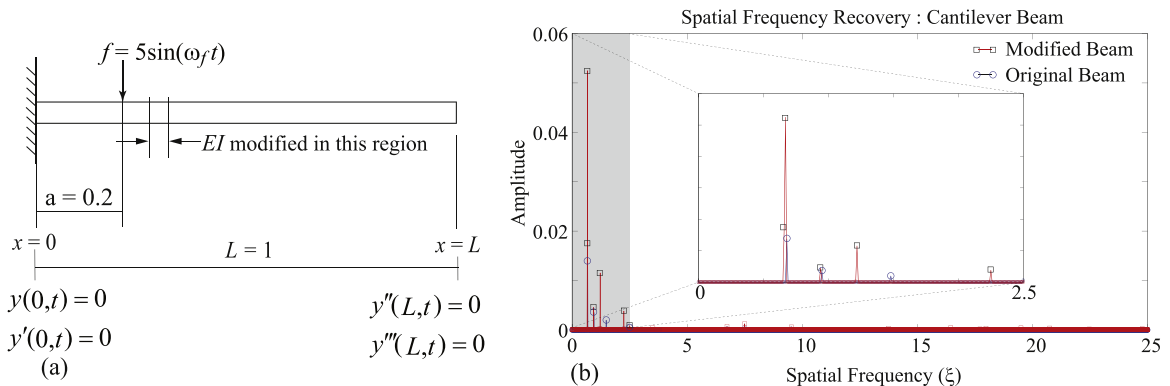


Fig. 13. (a) Schematic: Cantilever beam, (b) Spatial frequencies recovered from original and modified deflections.

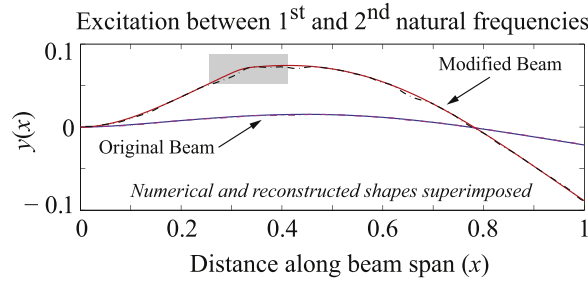


Fig. 14. Deflection shape reconstruction of original and modified cantilever beam.

were predominantly present in the response ($\xi \approx 0.5, 1$). Similarly, $k=6$ represents the case when the first 3 modes are predominantly present in the forced response of the beam. Contours in Fig. 12 match the trend of the contours in Fig. 6, thus reinforcing the following about ℓ_1 minimization in the spatial domain also: (i) Signal recovery is enhanced with increase in the number of measurements (ii) Higher sparsity benefits signal recovery and reconstruction.

6.3. Deflection shape reconstruction for cantilever beam

In this section, structural changes introduced in a cantilever beam are located by compressive sampling. The process closely follows that explained in the Sections 6.1 and 6.2. A schematic representation of a cantilever beam, with its boundary conditions, is shown in Fig. 13(a). Beam parameters retain the same value as prior sections, i.e. $L=1, \rho A=1, EI=1$ and the number of elements in the simulation model is $N_{el}=1000$. The harmonic force, applied at $a=0.5$, has a frequency of $\omega_f=20$ rad/s. From Eq. (5) and [65], the deflection equation for a cantilever beam, at any instant \bar{t} can be expressed as

$$y(x, \bar{t}) = \sum_{q=1}^{\infty} \bar{D}_q(\bar{t}) W_q, \quad W_q = (\sin \beta_q x - \sinh \beta_q x) - \alpha_q (\cos \beta_q x - \cosh \beta_q x),$$

$$\alpha_q = \frac{\sinh \beta_q L + \sin \beta_q L}{\cos \beta_q L + \cosh \beta_q L}, \quad \cos \beta_q L \cdot \cosh \beta_q L = -1. \tag{26}$$

For cantilever beams, Eq. (26) yields $[\beta_1 L, \beta_2 L, \beta_3 L, \dots] = [1.88, 4.69, 7.85, \dots]$. Thus, ω_f is between the first two natural frequencies, $\omega_1 = \beta_1^2 = 3.53$ rad/s and $\omega_2 = \beta_2^2 = 22$ rad/s. It is also noted that the spatial frequency $\xi_2 = \beta_2/(2\pi) = 0.75$. Based on Eq. (26), measurements z_j were expressed as in Eq. (22). The spatial frequency range for reconstruction was chosen as $\Xi_r = [\xi_l, \xi_h] = [0, 25]$, with a resolution of 0.01.

Unlike fixed-fixed beams where only *sinusoids* were used for the reconstruction, Eqs. (24) and (25), for cantilever beams consistent reconstruction required inclusion of the *hyperbolic* functions for lower frequencies. For a sub-set $\Xi_{r,h} = [0, 2.5]$ of Ξ_r , hyperbolics were included in the basis functions and for the remainder of Ξ_r , only sinusoids were used. The need of hyperbolics is expected for a cantilever beam since its deflections are neither perfectly sinusoidal (e.g. simply-supported beam), nor approximately sinusoidal (e.g. fixed-fixed beam). To simulate change, the rigidity modulus (EI) was reduced from 1 to 0.1 in the region $x \in [0.3, 0.35]$. The sparse solutions of the original and modified beam are shown in Fig. 13(b) and Fig. 14 illustrates reconstruction of the original and modified cantilever from the sparse solution. In solving the ℓ_1 minimum solution, the number of samples chosen was $m=25$ for the original beam and $m=35$ for the modified beam. Also, the amplitudes plotted in Fig. 13(b) are $\sqrt{\sum_{j=1}^4 H_{ij}^2}$.

7. Preliminary experimental validation

Section 5.2 explained compressive sensing based recovery of natural frequencies from the free vibration response of a cantilever beam. This section provides preliminary experimental validation for the same. The experimental setup is shown in Fig. 15(a), (b) and (c). The DAQ, amplifier and cantilever beam used in the setup are a part of an educational control systems module from QUANSER, which is used to study control concepts related to vibration analysis. For this experiment, the setup solely serves to acquire free vibration impulse response of the cantilever beam. The cantilever beam used is of mass $m=0.065$ kg, length $L=0.419$ m, width $b=0.02$ m and stiffness $K_{stiff} = 1.66$ kg m² (rad/s)². As indicated in Fig. 15(b), the beam consists of a strain gauge mounted at one end to measure the deflection when an impulse is experienced near the base (see Fig. 15(c)). The strain gauge used has a measurement range of -5 V to $+5$ V. The free vibration response of the unmodified cantilever beam at a sampling frequency of 1000 Hz is presented in Fig. 15(d).

Theoretically, the free vibration response of a beam will consist of all the natural frequencies (modes) of vibration. In practice, the lower modes are predominantly present in the free vibration response. This pattern of energy concentration in the lower modes (1st and 2nd) was observed in the experimental results. As a first step, the original natural frequencies of

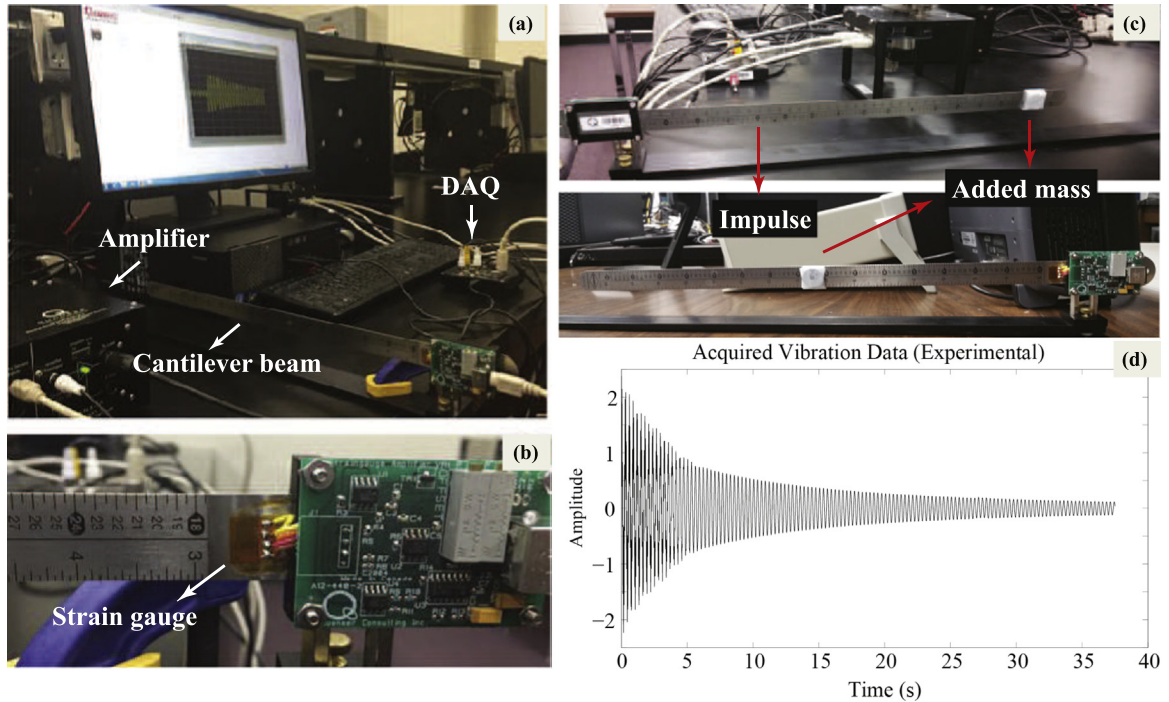


Fig. 15. (a) Experimental setup with all components (b) Strain gauge on beam (c) Point of application of impulse and added mass on beam (d) Acquired data from cantilever setup when no mass is added.

Table 1

Recovered natural frequencies of the cantilever beam with tip mass.

Added mass	% m increase	ω_1	% ω_1 drop	ω_2	% ω_2 drop
No mass added (Case 1)	–	3.387 Hz	–	21.25 Hz	–
2.4 g (Case 2)	3.7	3.17 Hz	6.3	20.67 Hz	2.7
4.9 g (Case 3)	7.5	2.99 Hz	11.7	20.29 Hz	4.5
6 g (Case 4)	9.2	2.91 Hz	14.2	20.16 Hz	5.1
9.8 g (Case 5)	15.1	2.72 Hz	19.7	19.73 Hz	7.1
15.2 g (Case 6)	23.4	2.48 Hz	26.8	19.25 Hz	9.4
30.4 g (Case 7)	46.8	2.053 Hz	39.4	18.64 Hz	12.3

Table 2

Recovered natural frequencies of the cantilever beam with mass at mid length.

Added mass	% m increase	ω_1	% ω_1 drop	ω_2	% ω_2 drop
No mass added (Case 1)	–	3.387 Hz	–	21.25 Hz	–
2.4 g (Case 2)	3.7	3.36 Hz	0.8	20.29 Hz	4.5
4.9 g (Case 3)	7.5	3.33 Hz	1.7	19.52 Hz	8.1
6 g (Case 4)	9.2	3.32 Hz	1.98	19.31 Hz	9.1
9.8 g (Case 5)	15.1	3.307 Hz	2.4	18.24 Hz	14.2
15.2 g (Case 6)	23.4	3.2 Hz	5.5	17.23 Hz	18.9
30.4 g (Case 7)	46.8	3.12 Hz	7.9	15.09 Hz	28.99

vibration of the unmodified beam were identified from its free vibration response using Fast Fourier Transform with the following problem setup: (i) Duration of data capture 37.5 s (ii) Sampling frequency 1 kHz (iii) Number of data points 37500 at regular intervals. The resulting first and second natural frequencies were 3.387 Hz and 21.25 Hz respectively.

Once the original frequencies were established as a known quantity, the beam characteristics were deliberately changed to investigate a shift in these natural frequencies. This change was incorporated by adding mass sets at two locations of the beam, each considered as an independent configuration: (i) Tip of the beam (ii) Mid length of the beam, as shown in Fig. 15

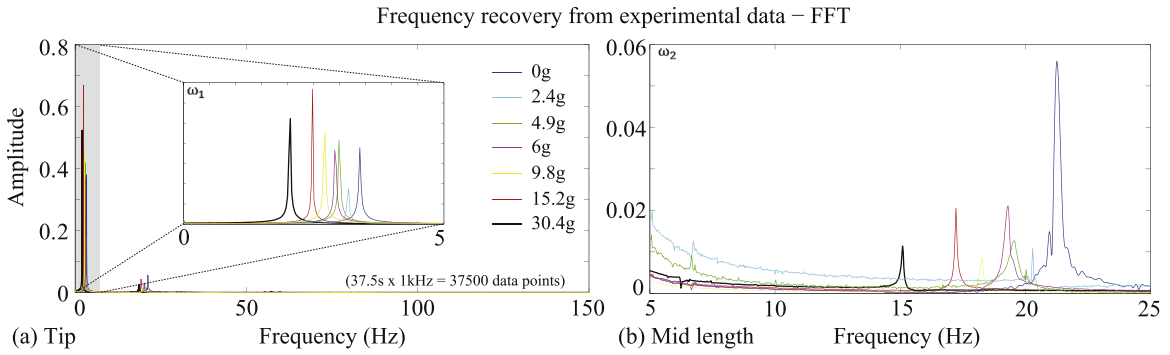


Fig. 16. Frequency recovery from experimental data of cantilever beam using FFT (a) Tip mass (ω_1 & ω_2) (b) Mass at mid length (ω_2).

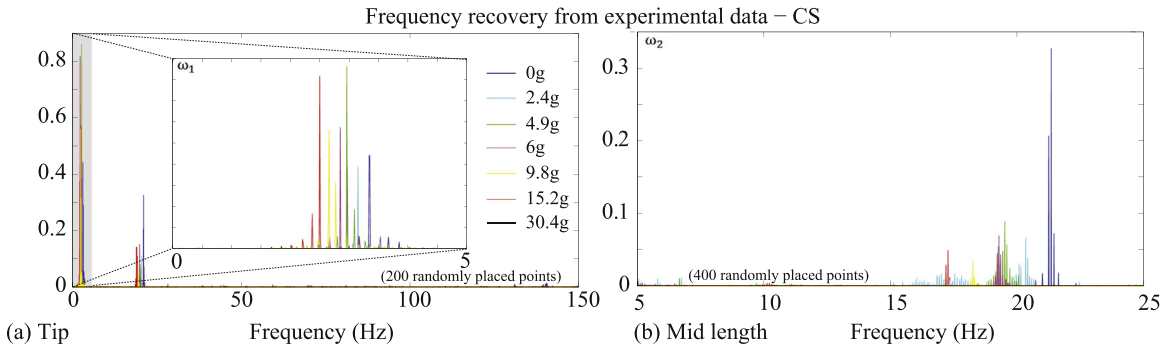


Fig. 17. Frequency recovery from experimental data of cantilever beam using CS (a) Tip mass (ω_1 and ω_2) (b) Mass at mid length (ω_2).

(c). In each configuration, 6 cases were investigated, each with a different value of added mass. Addition of masses introduced shift in natural frequencies of vibration, an effect similar to that produced when damage develops in a structure. Therefore, adding different values of masses may be analogous to varying levels of damage. The values of added mass, modified frequencies and percentage reduction for tip mass and mass at mid-length are listed in Tables 1 and 2 respectively.

In accordance with theory that increase in mass reduces the natural frequency of vibration, in each scenario, a left-shift was observed in the recovered frequencies (see Fig. 16 (a), (b)). However, from Table 2, it was observed that when mass sets were added at mid length of the beam, the reduction in second natural frequency was more evident than the first. Therefore, only the shift in ω_2 is shown for this case.

Fig. 17 illustrates compressive sensing based frequency recovery from the same free vibration responses for all the cases listed in Tables 1 and 2. The specifications of the CS problem setup were as follows: (i) Duration of data capture 0 – 5 s (ii) Frequency range in Hz, $N = 0: 0.01: 150$ (ii) Number of data points 200 (randomly spaced in time). When mass sets were added at mid length of the beam, recovery of the second natural frequencies were harder with just 200 data points. In order to ensure recovery, the number of random samples was increased to 400.

The experimental data contained noise. However, it may be observed from the results that the signal to noise ratio (SNR) was sufficient to recover the first and second natural frequencies from reduced number of samples using CS. Furthermore, their values matched those listed in Tables 1 and 2. Hence, CS promises to be a good candidate for reducing sensing and data requirement in vibration based monitoring of simple mechanical structures (Fig. 18).

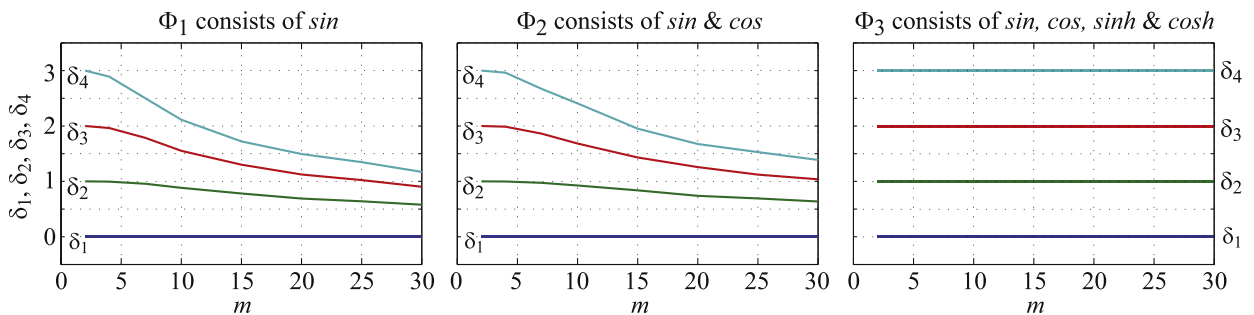


Fig. 18. Variation of δ_k with m for different measurement matrix ϕ .

8. Comparison of measurement matrices for RIP

Section 6 described the formulation and reconstruction results for locating changes in the ODS of simply-supported, fixed-fixed and cantilever beams using compressive sampling. The boundary conditions and hence the mode shape functions of these beams become increasingly complicated in that order [65]. It is observed that as hyperbolic functions become more prominent in mode shapes, the spatial data requirement increases for high quality reconstruction. The simply-supported beam only contains sinusoidal components in its mode shapes. Its measurement matrix Φ , shown in Eq. (20), produces consistent reconstruction in terms of fidelity and probability. While for the ODS of a fixed-fixed beam, Φ (see Eq. (25)) could be manipulated to containing only non-hyperbolic components, these hyperbolic functions became indispensable in the case of a cantilever beam. For either beams, it was important to eliminate or reduce the frequency range over which hyperbolic basis functions were used. Evidently, this is because of the non-periodic and unbounded nature of hyperbolic functions which makes the Φ matrix ill-conditioned. This can be linked to the requirement of Restricted Isometry Property (RIP) discussed in Section 4.2. Using Eq. (12), the Restricted Isometry Constant δ_k is calculated for Φ matrices with and without hyperbolic components. From Eq. (12), it is understood that calculating δ_k for any $m \times n$ matrix is a combinatorial task that becomes computationally intensive when n is large. However, to get an understanding of how the Φ matrices compare to one another with respect to probability of reconstruction (spatial domain), n is kept small and δ_k is numerically calculated for $k = 1, \dots, 4$. Specifically, $\Xi = [0, 5] \text{ m}^{-1}$ is chosen as the frequency range with a resolution of 0.01 m^{-1} . The individual spatial frequencies are therefore, $\xi_i = 5(i - 1)/(n - 1)$, $n = 51$, $i = 1, 2, \dots, n$. The measurement matrices are: $\Phi_1 \in R^{m \times n}$ containing only *sine* functions, $\Phi_2 \in R^{m \times 2n}$ containing both *sine* and *cosine* functions, and $\Phi_3 \in R^{m \times 4n}$ containing *sine*, *cosine*, *sinh* and *cosh* functions. The Φ_3 matrix is constructed as

$$\Phi_3 = \begin{bmatrix} \sin(2\pi\xi_1x_1) & \dots & \sin(2\pi\xi_nx_1) & \cos(2\pi\xi_1x_1) & \dots & \cos(2\pi\xi_nx_1) \\ \sin(2\pi\xi_1x_2) & \dots & \sin(2\pi\xi_nx_2) & \cos(2\pi\xi_1x_2) & \dots & \cos(2\pi\xi_nx_2) & \dots \\ \vdots & \vdots & \vdots & \vdots & \vdots & \vdots & \vdots \\ \sin(2\pi\xi_1x_m) & \dots & \sin(2\pi\xi_nx_m) & \cos(2\pi\xi_1x_m) & \dots & \cos(2\pi\xi_nx_m) \\ \sinh(2\pi\xi_1x_1) & \dots & \sinh(2\pi\xi_nx_1) & \cosh(2\pi\xi_1x_1) & \dots & \cosh(2\pi\xi_nx_1) \\ \dots & \sinh(2\pi\xi_1x_2) & \dots & \sinh(2\pi\xi_nx_2) & \cosh(2\pi\xi_1x_2) & \dots & \cosh(2\pi\xi_nx_2) \\ \vdots & \vdots & \vdots & \vdots & \vdots & \vdots & \vdots \\ \sinh(2\pi\xi_1x_m) & \dots & \sinh(2\pi\xi_nx_m) & \cosh(2\pi\xi_1x_m) & \dots & \cosh(2\pi\xi_nx_m) \end{bmatrix}. \quad (27)$$

The following are the results of δ_k for k ranging from 1 to 4, i.e. sparse vectors that have from 1 to 4 non-zero entries. In each of the above cases, although the number of frequencies remains the same, the size of Φ varies. In the first case, Φ_1 contains only sine components of all the frequencies. The matrix is well conditioned with δ_k showing steady reduction as the number of random samples m increases. This led to high probability of accurate ODS reconstruction for a simply-supported beam with few data points. The performance of Φ_2 is very similar to that of Φ_1 . This is expected since *sine* and *cosine* functions are bounded and periodic with similar magnitudes. The matrix Φ_3 presents a more complicated case. It can be observed that in contrast to Φ_1 and Φ_2 , all the calculated δ_k 's are integer values and non-decreasing, indicating a computational shortcoming. This can be attributed to the presence of hyperbolic components in Φ_3 . These unbounded and non-periodic functions contribute to the ill-conditioning of the matrix, thus leading to inexact or failure of reconstruction in the ODS reconstruction of a cantilever beam. Recall from Section 6.3 that for the cantilever beam, the frequency range of the hyperbolic functions was reduced and this helped in improving the probability of accurate reconstruction.

9. Conclusion and future scope

This paper shows the application of CS in vibration-based monitoring of mechanical structures. To demonstrate its viability, this study focuses on lateral vibration of fundamental beams such as simply-supported, fixed-fixed and cantilever beams. Recovery of natural frequencies from free vibration data using CS is demonstrated, which enables fault detection. The inherent sparsity in frequency domain is exploited by CS to enable accurate recovery from random and under-sampled data. Subsequently, CS is extended to spatial domain and used to reconstruct ODS from random spatially distributed vibration data. This step can potentially help locate a fault. Here again, sparsity of mode shapes is utilized by CS to deliver accurate reconstruction with limited sensing. In addition to simulation results that demonstrated the feasibility of CS-based detection and localization of fault, preliminary experimental validation for detecting shift in natural frequencies of a cantilever beam is presented. CS-based recovery was tested for two configurations of structural change (tip and mid-length), each with six different values of added mass. The shift in natural frequencies thus produced followed a trend similar to that expected due to varying levels of damage. In these experiments, CS based recovery was feasible without explicit formulation for handling of noise in the ℓ_1 minimization problem. Also, filtering of noise was not required. However, more complex structures may have amplitudes of vibration comparable to noise, which might warrant explicit formulation of noise in the ℓ_1 minimization problem. This aspect of CS will be examined as an extension of this work. This paper provides a fundamental and initial effort in applying CS to vibration based diagnostics and monitoring, and further research is needed in

many fronts. Combined spatio-temporal CS, optimized sensor placement, extension to complicated structures, and improved robustness of recovery/reconstruction, are some of the future directions to be pursued.

References

- [1] Z.Y. Shi, S.S. Law, L.M. Zhang, Structural damage detection from modal strain energy change, *J. Eng. Mech.* 126 (12) (2000) 1216–1223.
- [2] S.W. Doebbling, C.R. Farrar, M.B. Prime, D.W. Shevitz, Damage identification and health monitoring of structural and mechanical systems from changes in their vibration characteristics: A literature review, Tech. rep., Los Alamos National Lab., NM, USA, 1996.
- [3] N. Tandon, A. Choudhury, A review of vibration and acoustic measurement methods for the detection of defects in rolling element bearings, *Tribol. Int.* 32 (8) (1999) 469–480.
- [4] A. Ghoshal, M.J. Sundaresan, M.J. Schulz, P.F. Pai, Structural health monitoring techniques for wind turbine blades, *J. Wind Eng. Ind. Aerodyn.* 85 (3) (2000) 309–324.
- [5] A.E. Aktan, F.N. Catbas, K.A. Grimmelsman, C.J. Tsikos, Issues in infrastructure health monitoring for management, *J. Eng. Mech.* 126 (7) (2000) 711–724.
- [6] F.N. Catbas, A.E. Aktan, Condition and damage assessment: issues and some promising indices, *J. Struct. Eng.* 128 (8) (2002) 1026–1036.
- [7] F.N. Catbas, H.B. Gokce, M. Gul, Nonparametric analysis of structural health monitoring data for identification and localization of changes: concept, lab, and real-life studies, *Struct. Health Monit.* 11 (5) (2012) 613–626.
- [8] E.P. Carden, P. Fanning, Vibration based condition monitoring: a review, *Struct. Health Monit.* 3 (4) (2004) 355–377.
- [9] C.R. Farrar, S.W. Doebbling, Damage detection and evaluation ii: field applications to large structures, in: J.M.M. Silva, N.M.M. Maia (Eds.), *Modal Analysis and Testing*, Springer, 1999.
- [10] R.D. Adams, P. Cawley, C.J. Pye, B.J. Stone, A vibration technique for non-destructively assessing the integrity of structures, *J. Mech. Eng. Sci.* 20 (2) (1978) 93–100.
- [11] M.M. Samman, M. Biswas, Vibration testing for nondestructive evaluation of bridges. i: theory, *J. Struct. Eng.* 120 (1) (1994) 269–289.
- [12] M.M. Samman, M. Biswas, Vibration testing for nondestructive evaluation of bridges. ii: results, *J. Struct. Eng.* 120 (1) (1994) 290–306.
- [13] A.E. Aktan, D.N. Farhey, A.J. Helmicki, D.L. Brown, V.J. Hunt, K.-L. Lee, A. Levi, Structural identification for condition assessment: experimental arts, *J. Struct. Eng.* 123 (12) (1997) 1674–1684.
- [14] L. Fryba, M. Pirner, Load tests and modal analysis of bridges, *Eng. Struct.* 23 (1) (2001) 102–109.
- [15] N.M.M. Maia, J.M.M. Silva, *Theoretical and Experimental Modal Analysis*, Research Studies Press Ltd., 1997.
- [16] P. Cawley, R.D. Adams, The location of defects in structures from measurements of natural frequencies, *J. Strain Anal. Eng. Des.* 14 (2) (1979) 49–57.
- [17] O.S. Salawu, Detection of structural damage through changes in frequency: a review, *Eng. Struct.* 19 (9) (1997) 718–723.
- [18] H.T. Banks, D.J. Inman, D.J. Leo, Y. Wang, An experimentally validated damage detection theory in smart structures, *J. Sound Vib.* 191 (5) (1996) 859–880.
- [19] S.S. Kessler, S.M. Spearing, M.J. Atalla, C.E.S. Cesnik, C. Soutis, Damage detection in composite materials using frequency response methods, *Compos. Part B: Eng.* 33 (1) (2002) 87–95.
- [20] H.L. Chen, C.C. Spyarakos, G. Venkatesh, Evaluating structural deterioration by dynamic response, *J. Struct. Eng.* 121 (8) (1995) 1197–1204.
- [21] P.C. Chang, A. Faltau, S. Liu, Review paper: health monitoring of civil infrastructure, *Struct. Health Monit.* 2 (3) (2003) 257–267.
- [22] C.R. Farrar, W.E. Baker, T.M. Bell, K.M. Cone, T.W. Darling, T.A. Duffey, A. Migliori, Dynamic characterization and damage detection in the i-40 bridge over the rio grande, Tech. rep., Los Alamos National Lab., NM (United States), 1994.
- [23] S.S. Law, H.S. Ward, G.B. Shi, R.Z. Chen, P. Waldron, C. Taylor, Dynamic assessment of bridge load-carrying capacities. i, *J. Struct. Eng.* 121 (3) (1995) 478–487.
- [24] S.S. Law, H.S. Ward, G.B. Shi, R.Z. Chen, P. Waldron, C. Taylor, Dynamic assessment of bridge load-carrying capacities. ii, *J. Struct. Eng.* 121 (3) (1995) 488–495.
- [25] J.A. Pereira, W. Heylen, S. Lammens, P. Sas, Influence of the number of frequency points and resonance frequencies on modal updating techniques for health condition monitoring and damage detection of flexible structure, in: Proceedings-SPIE The International Society for Optical Engineering, 1995, pp. 1273–1273.
- [26] J.A. Pereira, W. Heylen, S. Lammens, P. Sas, Model updating and failure detection based on experimental frf's: Case study on a space frame structure, in: Proceedings of the International Conference on Noise and Vibration Engineering, 1994, pp. 669–681.
- [27] M.A. Mannan, M.H. Richardson, Detection and location of structural cracks using FRF measurements, in: Proceedings of the 8th International Modal Analysis Conference, , vol. 1, 1990, pp. 652–657.
- [28] A. Morassi, Identification of a crack in a rod based on changes in a pair of natural frequencies, *J. Sound Vib.* 242 (4) (2001) 577–596.
- [29] I. Trendafilova, W. Heylen, Fault localization in structures from remote frf measurements. influence of the measurement points, in: Proceedings of the International Conference on Noise and Vibration Engineering, Leuven, Belgium, 1998, pp. 149–156.
- [30] D.J. Ewins, *Modal Testing: Theory and Practice*, 2nd ed. Research Studies Press Ltd., 2000.
- [31] R.J. Allemang, D.L. Brown, A correlation coefficient for modal vector analysis, in: Proceedings of the 1st International Modal Analysis Conference, Orlando, FL, , vol. 1, 1982, pp. 110–116.
- [32] N.A.J. Lieven, D.J. Ewins, Spatial correlation of mode shapes, the coordinate modal assurance criterion (COMAC), in: Proceedings of the 4th International Modal Analysis Conference, , vol. 1, 1988, pp. 690–695.
- [33] J.Chance, J.R. Tomlinson, K. Worden, A simplified approach to the numerical and experimental modelling of the dynamics of a cracked beam, SPIE Vol. 2251, in: Proceedings of the 12th International Modal Analysis Conference (1994) 778–785.
- [34] W.-X. Ren, G. de Roeck, Structural damage identification using modal data. i: simulation verification, *J. Struct. Eng.* 128 (1) (2002) 87–95.
- [35] W.-X. Ren, G. de Roeck, Structural damage identification using modal data. ii: test verification, *J. Struct. Eng.* 128 (1) (2002) 96–104.
- [36] S. Alampalli, G. Fu, E.W. Dillon, Signal versus noise in damage detection by experimental modal analysis, *J. Struct. Eng.* 123 (2) (1997) 237–245.
- [37] C.P. Ratcliffe, W.J. Bagaria, Vibration technique for locating delamination in a composite beam, *AIAA J.* 36 (6) (1998) 1074–1077.
- [38] M.M.A. Wahab, G. de Roeck, Damage detection in bridges using modal curvatures: application to a real damage scenario, *J. Sound Vib.* 226 (2) (1999) 217–235.
- [39] B. Oh, B. Jung, Structural damage assessment with combined data of static and modal tests, *J. Struct. Eng.* 124 (8) (1998) 956–965.
- [40] M.M.A. Wahab, Effect of modal curvatures on damage detection using model updating, *Mech. Syst. Signal Process.* 15 (2) (2001) 439–445.
- [41] R.P.C. Sampaio, N.M.M. Maia, J.M.M. Silva, Damage detection using the frequency-response-function curvature method, *J. Sound Vib.* 226 (5) (1999) 1029–1042.
- [42] J.-T. Kim, N. Stubbs, Model-uncertainty impact and damage-detection accuracy in plate girder, *J. Struct. Eng.* 121 (10) (1995) 1409–1417.
- [43] O.S. Salawu, C. Williams, Bridge assessment using forced-vibration testing, *J. Struct. Eng.* 121 (2) (1995) 161–173.
- [44] Z.Y. Shi, S.S. Law, L.M. Zhang, Damage localization by directly using incomplete mode shapes, *J. Eng. Mech.* 126 (6) (2000) 656–660.
- [45] P.F. Pai, L.G. Young, Damage detection of beams using operational deflection shapes, *Int. J. Solids Struct.* 38 (18) (2001) 3161–3192.
- [46] K. Waldron, A. Ghoshal, M.J. Schulz, M.J. Sundaresan, F. Ferguson, P.F. Pai, J.H. Chung, Damage detection using finite element and laser operational deflection shapes, *Finite Elem. Anal. Des.* 38 (3) (2002) 193–226.
- [47] T.J. Johnson, D.E. Adams, Transmissibility as a differential indicator of structural damage, *J. Vib. Acoust.* 124 (4) (2002) 634–641.
- [48] F.N. Catbas, H.B. Gokce, M. Gul, Nonparametric analysis of structural health monitoring data for identification and localization of changes: concept, lab, and real-life studies, *Struct. Health Monit.* (2012). (1475921712451955).

- [49] A. Raghavan, C.E.S. Cesnik, Review of guided-wave structural health monitoring, *Shock Vib. Dig.* 39 (2007) 91–114.
- [50] M. Wu, X. Chen, C.R. Liu, Highway crack monitoring system, in: SPIE's Proceedings of the 9th Annual International Symposium on Smart Structures and Materials, 2002, pp. 293–299.
- [51] M. Solís, M. Algaba, P. Galvín, Continuous wavelet analysis of mode shapes differences for damage detection, *Mech. Syst. Signal Process.* 40 (2) (2013) 645–666.
- [52] M. Rucka, K. Wilde, Crack identification using wavelets on experimental static deflection profiles, *Eng. Struct.* 28 (2) (2006) 279–288.
- [53] U.P. Poudel, G. Fu, J. Ye, Structural damage detection using digital video imaging technique and wavelet transformation, *J. Sound Vib.* 286 (4) (2005) 869–895.
- [54] A. Messina, Refinements of damage detection methods based on wavelet analysis of dynamical shapes, *Int. J. Solids Struct.* 45 (14) (2008) 4068–4097.
- [55] Q. Wang, X. Deng, Damage detection with spatial wavelets, *Int. J. Solids Struct.* 36 (23) (1999) 3443–3468.
- [56] L. Montanari, B. Basu, A. Spagnoli, B.M. Broderick, A padding method to reduce edge effects for enhanced damage identification using wavelet analysis, *Mech. Syst. Signal Process.* 52 (2015) 264–277.
- [57] M. Unser, Sampling—50 years after Shannon, *Proc. IEEE* 88 (4) (2000) 569–587.
- [58] R.G. Baraniuk, More is less: signal processing and the data deluge, *Science* 331 (6018) (2011) 717–719.
- [59] L. Montanari, A. Spagnoli, B. Basu, B. Broderick, On the effect of spatial sampling in damage detection of cracked beams by continuous wavelet transform, *J. Sound Vib.* 345 (2015) 233–249.
- [60] M. Fornasier, H. Rauhut, Compressive sensing, in: Handbook of mathematical methods in imaging, Springer, 2011, pp. 187–228.
- [61] Y. Bao, J.L. Beck, H. Li, Compressive sampling for accelerometer signals in structural health monitoring, Structural Health Monitoring.
- [62] G. Chardon, A. Leblanc, L. Daudet, Plate impulse response spatial interpolation with sub-nyquist sampling, *J. sound Vib.* 330 (23) (2011) 5678–5689.
- [63] I. Dokmanić, M. Vetterli, Room helps: Acoustic localization with finite elements, in: Proceedings of the 2012 IEEE International Conference on Acoustics, Speech and Signal Processing (ICASSP), Ieee, 2012, pp. 2617–2620.
- [64] G. Chardon, T. Nowakowski, J. de Rosny, L. Daudet, A blind dereverberation method for narrowband source localization, *IEEE J. Sel. Top. Signal Process.* 9 (5) (2015) 815–824.
- [65] S.S. Rao, *Mechanical Vibrations*, 5th ed. Prentice Hall, 2011.
- [66] B.M. Sanandaji, T.L. Vincent, K. Poolla, M.B. Wakin, A tutorial on recovery conditions for compressive system identification of sparse channels, in: 2012 IEEE Proceedings of the 51st Annual Conference on Decision and Control (CDC), IEEE, 2012, pp. 6277–6283.
- [67] S. Boyd, L. Vandenberghe, *Convex Optimization*, Cambridge University Press, 2004.
- [68] E. J. Candès, Compressive sampling, in: Proceedings of the International Congress of Mathematicians, , vol. 3, Madrid, Spain, 2006, pp. 1433–1452.
- [69] ℓ_1 -magic, (<http://statweb.stanford.edu/~candes/l1magic/>).
- [70] S. Foucart, H. Rauhut, *A Mathematical Introduction to Compressive Sensing*, Springer, 2013.
- [71] S.F. Franklin, J.D. Powell, M.L. Workman, *Digital Control of Dynamic Systems*, Ellis-Kagle Press, 1997.